arXiv:1607.01829v1 [astro-ph.SR] 6 Jul 2016

Version 2; 05/31/2016

The Hot Companion and Circumbinary Disk of the Be Star HR 2142

Geraldine J. Peters[1,2]

Space Sciences Center, University of Southern California, Los Angeles, CA 90089-1341, USA; gpeters@usc.edu

Luqian Wang, Douglas R. Gies

Center for High Angular Resolution Astronomy and Department of Physics and Astronomy, Georgia State University, P. O. Box 5060, Atlanta, GA 30302-5060, USA; lwang@chara.gsu.edu, gies@chara.gsu.edu

Erika D. Grundstrom[2]

Physics and Astronomy Department, Vanderbilt University, 6301 Stevenson Center, Nashville, TN 37235, USA; erika.grundstrom@vanderbilt.edu

ABSTRACT

We present a spectroscopic investigation of the Be+sdO binary system HR 2142 that is based upon large sets of ultraviolet observations from the *International Ultraviolet Explorer* and ground-based Hα observations. We measured radial velocities for the Be star component from these spectra, and computed a revised orbit. In order to search for the spectral signature of the hot subdwarf, we cross-correlated the short wavelength end of each *IUE* spectrum with a model hot star spectrum, and then we used the predicted Doppler shifts of the subdwarf to shift-and-add all the cross-correlation functions to the frame of the subdwarf. This merged function shows the weak signal from the spectral lines of the hot

[1]Guest Observer with the *International Ultraviolet Explorer Satellite*.

[2]Visiting Astronomer, Kitt Peak National Observatory, National Optical Astronomy Observatory, operated by the Association of Universities for Research in Astronomy, Inc., under contract with the National Science Foundation.

star, and a best fit is obtained with a mass ratio $M_2/M_1 = 0.07 \pm 0.02$, companion temperature $T_{\rm eff} \geq 43 \pm 5$ kK, projected rotational velocity $V \sin i < 30$ km s^{-1}, and a monochromatic flux ratio near 1170 Å of $f_2/f_1 > 0.009 \pm 0.001$. This hot subdwarf creates a one-armed spiral, tidal wake in the disk of the Be star, and we present a circumbinary disk model that can explain the occurrence of shell absorption lines by gas enhancements that occur where gas crossing the gap created by the subdwarf strikes the disk boundaries. The faint companion of HR 2142 may be representative of a significant fraction of Be stars with undetected **former** mass donor companion stars.

Subject headings: stars: emission-line, Be — stars: individual (HR 2142, HD 41335) — stars: binaries: spectroscopic — stars: evolution — stars: subdwarfs

1. Introduction

Close binary stars are progressively more common among stars of higher mass (Duchêne & Kraus 2013), so we expect that binary interactions will play a fundamental role in the evolution of a significant fraction of massive stars (de Mink et al. 2014). Roche lobe overflow (RLOF) in close binaries with extreme mass ratios may lead to mergers or a common envelope stage, but in systems with comparable mass stars, RLOF can proceed in a stable manner in which the mass donor star eventually becomes stripped down to a much lower mass (Wellstein et al. 2001). RLOF provides mass and angular momentum to the mass gainer star, so that products of binary interaction may appear as a population of rapidly rotating stars (de Mink et al. 2014). Pols et al. (1991) first suggested that such mass gainers might be associated with the rapidly rotating Be stars, emission-line stars surrounded by out-flowing circumstellar disks (Rivinius et al. 2013). This idea is supported by the fact that most of the massive X-ray binaries consist of a Be star with an orbiting neutron star companion, the remnant of a massive donor star (Reig 2011). However, mass donors below the Chandrasekhar limit will appear as hot subdwarfs or white dwarfs, and such systems with faint companions may account for a large fraction of Be stars (Shao & Li 2014).

Detection of such faint, subdwarf companions to Be stars is difficult because of the huge flux contrast between the Be star and companion. The stripped down donor stars are expected to be much hotter than the Be stars, so detection is favored in the ultraviolet part of the spectrum where the flux ratio increases. In fact, the first **direct spectroscopic** detection of a hot subdwarf companion of the Be star ϕ Per was made by Thaller et al. (1995) through investigation of ultraviolet (UV) spectra made with the *International Ultraviolet Explorer (IUE)* satellite. The nature of the companion was revealed in subsequent

UV spectroscopy from *Hubble Space Telescope* (Gies et al. 1998), and recent interferometric observations with the CHARA Array have led to an astrometric orbit and masses for the ϕ Per system (Mourard et al. 2015). Encouraged by the UV detection of the companion of ϕ Per, we subsequently launched an investigation of the UV spectra of Be binaries that were frequently observed by *IUE*, and our work led to the discovery of the hot subdwarf companions of FY CMa (Peters et al. 2008) and 59 Cyg (Peters et al. 2013). The presence of a hot companion in ϕ Per was first suggested by emission line variations caused by heating of the Be star's disk gas by the hot companion (Poeckert 1981; Hummel & Štefl 2001), and observations of similar emission line variations may indicate the presence of hot subdwarf companions to the Be stars *o* Pup (Koubský et al. 2012) and HD 161306 (Koubský et al. 2014).

Here we turn our attention to the Be binary HR 2142, another system with an excellent set of UV spectra in the *IUE* archive. The spectroscopic emission features of HR 2142 (HD 41335, V696 Mon; B1.5 IV-Vnne) were first noted by Campbell (1895), and it has since attracted much attention among spectroscopists because of its strong Balmer emission lines that vary periodically in a predictable manner. Peters (1971) observed the development of strong absorption components in the Balmer lines, and their cyclic appearance led Peters (1972) to propose that these shell-type absorptions occur during a short part of the orbit in a binary system. Subsequent optical spectroscopy by Peters (1983) confirmed the binary nature of HR 2142 through measurement of the radial velocity variations associated with the orbital period of $P = 80.86$ days. Early observations with *IUE* demonstrated that many transitions in the UV also displayed the shell line variations found in the Balmer lines (Peters 2001). Waters et al. (1991) examined the spectral energy distribution of HR 2142 in the infrared and showed that the companion cannot be a cool giant (as found in Algol binaries). Instead, they proposed that the companion is a hot subdwarf or "helium star", the stripped down remains of the donor star in this interacting binary. Thus, HR 2142 is a prime candidate for detection of a hot companion through a search for its flux contribution in the UV.

This paper presents the results of our analysis of the collection of the *IUE* spectra of HR 2142. Section 2 describes the UV spectra and a large sample of complementary Hα spectroscopy. We present radial velocities of the bright Be star component measured from these spectra, and we calculate an updated radial velocity curve from these data. Section 3 describes our cross-correlation analysis of the far-UV part of the spectrum that provides the first positive evidence of the existence of a hot subdwarf companion. In Section 4, we document the appearance of the shell line variations in the UV and Hα, and we argue in Section 5 that these shell episodes result from tidal wakes in the disk of the Be star that are caused by the gravitational force of the companion. Our results are summarized in Section 6.

Preliminary results of this study appeared earlier in several conference proceedings (Peters 2001; Peters & Gies 2002; Peters et al. 2015).

2. Radial Velocities and Orbital Solution

The first step in this investigation was to revisit the orbital radial velocity curve of the Be star in order to establish a contemporary ephemeris and to verify the orbital semiamplitude. Radial velocity measurements were made using the set of spectra summarized in Table 1, which lists the source, number of spectra N, spectral resolving power and range, dates of observation, and primary observer. The main focus of this work is a set of 88 high resolution, SWP HIRES FUV spectra acquired over the lifetime of the *IUE* observatory. These were downloaded from MAST[3] and resampled on a uniform grid of heliocentric wavelength in $\log \lambda$ and rectified to a unit pseudo-continuum. We also collected a set of 49 LWR and LWP near-UV spectra that were used to inspect the orbital variations in the Mg II $\lambda\lambda 2796, 2803$ feature. The UV spectra were supplemented with a large collection of Hα spectra that we secured with the KPNO Coude Feed telescope and that were obtained by amateur astronomers participating in the Be Star Spectra database project (Pollmann 2007; Neiner et al. 2011).

Measurement of the radial velocity for individual line transitions is very difficult in the UV because the line spectrum is dense and strongly blended due to the large projected rotational broadening of the Be star's spectrum ($V \sin i = 358$ km s^{-1}; Frémat et al. 2005). Instead, we followed our well-honed method of determining the radial velocity through cross-correlation with a spectral template (Peters et al. 2013). We used the average spectrum as

[3]https://archive.stsci.edu/iue/

Table 1. Spectroscopic Observations of HR 2142

Code	Source	N	$\lambda/\Delta\lambda$	λ Range (Å)	Dates (BY)	Observer
1	Lick 3 m	50	10000–15000	3200–4700	1969–1975	Peters
2	IUE	88	12000	1150–1950	1978–1995	Peters **& others**
3	KPNO CFT	84	12000–25000	6400–6700	1985–2001	Peters
4	KPNO CFT	8	9500	6430–7140	2004–2008	Grundstrom
5	BeSS	41	> 10000	6563:	2006–2015	various

the template to form the cross-correlation function (CCF) in order to derive relative radial velocity shifts. The calculation omitted wavelength regions at the extreme wavelength ends, regions with broad wind lines, and sections with deep, narrow lines (formed in the interstellar medium and/or circumbinary disk). The derived CCFs were very broad as expected for the photospheric spectrum of the Be star, but still displayed a narrow peak at the core due to correlations among some remaining sharp lines. Consequently, we measured a bisector velocity of the wings of the CCF using a convolution with oppositely-signed Gaussian functions to sample the wing distribution (Shafter et al. 1986).

The Hα emission line is strong and formed over a large volume of the Be star disk. However, we can safely assume that the extreme wings of the emission line are formed in the part of the disk closest to the Be star, so that radial velocity variations of the wings reflect the motion of the Be star itself. Once again we determined a bisector velocity for the Hα emission line wings using a convolution with oppositely-signed Gaussian functions. These Hα emission line velocities are listed in Table 2 (given in full as a Machine Readable Table in the electronic version) that lists heliocentric Julian date of mid-exposure, the corresponding orbital phase (see below), the radial velocity, its uncertainty, the observed minus calculated velocity residual from the orbital solution, and a spectrum source code (associated with Table 1).

Table 2. Be Star Radial Velocities

Date (HJD-2400000)	Orbital Phase	V_r (km s^{-1})	σ (km s^{-1})	$O-C$ (km s^{-1})	Source Code[a]
40520.03	0.830	57.1	6.0	5.0	1
40527.05	0.917	56.8	12.2	7.4	1
40544.94	0.138	41.7	14.0	1.3	1
40572.94	0.484	47.9	23.3	2.8	1
40611.80	0.964	49.9	13.4	2.5	1
40637.73	0.285	37.5	7.0	−1.4	1
40638.63	0.296	36.2	16.0	−2.8	1
40659.61	0.555	45.8	15.9	−2.5	1
40850.04	0.908	55.2	10.7	5.5	1
40877.96	0.254	41.9	11.6	3.2	1
40903.92	0.574	55.8	4.5	6.7	1
40996.68	0.721	58.0	11.0	5.1	1
41200.04	0.234	34.9	14.7	−3.8	1
41228.06	0.580	48.5	14.0	−0.8	1
41236.04	0.679	60.5	9.6	8.2	1
41256.98	0.938	49.1	9.5	0.5	1
41256.98	0.938	51.5	8.4	2.9	1
41261.00	0.987	47.6	6.2	1.2	1
41261.00	0.987	42.2	10.7	−4.2	1
41346.70	0.047	44.8	8.2	1.0	1
41346.70	0.047	42.3	11.3	−1.5	1
41374.67	0.392	35.3	19.3	−6.1	1
41404.62	0.762	56.0	12.8	3.0	1
41406.63	0.787	50.7	10.3	−2.1	1
41433.65	0.121	34.5	17.0	−6.4	1
41590.04	0.054	38.9	6.5	−4.6	1
41591.00	0.066	40.2	14.1	−2.8	1
41614.94	0.362	38.0	18.0	−2.4	1
41616.96	0.387	34.6	18.4	−6.6	1
41643.98	0.721	50.3	11.1	−2.6	1
41644.89	0.732	47.4	11.3	−5.5	1
41644.90	0.732	49.8	12.0	−3.1	1
41936.02	0.330	34.4	6.9	−5.2	1
41975.00	0.812	52.9	25.0	0.5	1
41987.02	0.960	40.5	8.5	−7.1	1
41987.97	0.972	51.0	8.6	3.9	1
41990.95	0.009	48.8	16.7	3.4	1
41991.90	0.021	44.1	18.0	−0.8	1
41992.07	0.023	44.3	14.5	−0.5	1
42036.87	0.576	49.2	35.9	0.1	1
42083.73	0.156	36.8	14.5	−3.1	1
42149.65	0.970	44.9	6.9	−2.3	1
42312.02	0.977	40.0	8.8	−6.9	1
42316.97	0.038	52.4	8.9	8.3	1
42317.03	0.039	45.7	11.1	1.6	1

Table 2—Continued

Date (HJD-2400000)	Orbital Phase	V_r (km s^{-1})	σ (km s^{-1})	$O-C$ (km s^{-1})	Source Code[a]
42317.98	0.051	45.7	9.0	2.1	1
42317.98	0.051	44.0	11.3	0.4	1
42318.97	0.063	37.4	3.5	−5.7	1
42682.01	0.550	54.4	17.9	6.4	1
42733.94	0.191	40.9	24.0	1.7	1
43742.3180	0.654	54.7	6.6	3.0	2355
43808.2337	0.468	56.7	7.6	12.3	3162
43844.1164	0.912	63.0	7.5	13.4	3505
43848.1808	0.962	46.0	8.9	−1.5	3537
44167.1164	0.904	43.9	9.2	−6.0	6929
44169.9608	0.939	52.4	9.8	3.9	6961
44169.9955	0.939	49.2	6.5	0.8	6962
44172.0051	0.964	41.3	5.3	−6.1	6991
44173.7810	0.986	49.3	5.6	2.9	7007
44328.5142	0.899	57.2	5.5	7.1	8596
44328.5478	0.899	58.8	5.6	8.7	8597
44329.2100	0.907	52.1	5.7	2.3	8604
44330.1423	0.919	53.5	6.4	4.2	8616
44332.4697	0.947	43.0	6.9	−5.2	8637
44483.8703	0.819	51.2	5.5	−1.1	9978
44485.8594	0.843	42.5	5.4	−9.2	9992
44511.0631	0.155	47.6	6.1	7.6	10240
44533.7852	0.436	40.2	5.5	−2.8	10436
44612.3243	0.406	37.1	5.1	−4.8	10993
44616.4285	0.457	39.0	5.1	−4.9	11026
44661.2357	0.011	47.9	5.0	2.6	13359
44867.9669	0.566	63.0	5.2	14.3	15054
44891.3648	0.855	59.2	6.3	7.7	15255
44920.7181	0.218	37.4	5.7	−1.4	15477
44972.5984	0.859	57.5	6.1	6.1	15932
44974.5335	0.883	51.2	5.7	0.6	15955
44975.6692	0.897	48.4	5.4	−1.8	15977
45042.6617	0.725	64.5	6.9	11.6	16526
46121.7891	0.062	46.8	1.1	3.7	3
46122.6951	0.073	41.5	1.1	−1.1	3
46122.7103	0.073	42.0	1.3	−0.6	3
46152.6593	0.443	41.6	7.5	−1.7	3
46338.9463	0.745	64.7	5.5	11.8	26809
46734.9250	0.639	55.5	4.2	4.2	3
46737.7984	0.675	54.0	2.3	1.8	3
46820.6364	0.699	51.0	5.2	−1.6	30156
46823.6438	0.736	47.4	5.5	−5.6	30179
46824.5968	0.747	51.5	5.1	−1.5	30188
46826.6402	0.773	63.1	6.0	10.2	30207
46826.6638	0.773	55.7	5.1	2.8	30208

Table 2—Continued

Date (HJD-2400000)	Orbital Phase	V_r (km s^{-1})	σ (km s^{-1})	$O-C$ (km s^{-1})	Source Code[a]
46826.6978	0.773	54.7	5.7	1.8	30209
46826.7272	0.774	58.4	5.7	5.5	30210
46826.7616	0.774	65.8	5.6	12.9	30211
46826.7876	0.775	57.4	5.4	4.5	30212
46828.5744	0.797	55.4	4.9	2.7	30228
46828.6136	0.797	53.1	5.1	0.5	30229
46828.6442	0.797	44.7	6.5	−7.9	30230
46828.6690	0.798	52.2	5.3	−0.4	30231
46828.6952	0.798	44.9	5.2	−7.7	30232
46830.5249	0.821	52.8	5.5	0.6	30250
46832.5591	0.846	60.0	6.7	8.3	30263
46875.5064	0.377	48.7	5.3	7.8	30580
46875.5362	0.377	42.5	4.6	1.6	30581
46875.5655	0.377	43.6	5.0	2.7	30582
46875.5925	0.378	49.8	4.8	8.9	30583
46901.6395	0.700	57.3	3.0	4.7	3
46901.6452	0.700	59.1	3.4	6.5	3
46902.6503	0.712	59.4	1.5	6.6	3
46903.6545	0.725	59.6	3.0	6.7	3
46905.6139	0.749	56.7	1.1	3.7	3
46918.6402	0.910	47.8	9.7	−1.9	3
46919.6238	0.922	53.4	3.5	4.2	3
46919.6287	0.922	54.4	6.8	5.2	3
46920.6564	0.935	54.2	6.5	5.6	3
47030.9707	0.298	28.4	7.9	−10.6	3
47030.9854	0.298	51.5	7.8	12.4	3
47032.9747	0.323	50.3	6.8	10.9	3
47033.9595	0.335	50.2	5.7	10.6	3
47033.9629	0.335	39.3	6.5	−0.4	3
47103.9017	0.199	29.2	4.8	−9.8	32224
47141.6472	0.666	52.6	6.1	0.6	32507
47169.4943	0.010	44.1	5.8	−1.2	32687
47172.4692	0.047	47.8	5.8	4.1	32701
47198.4327	0.368	48.4	5.3	7.8	32874
47215.4720	0.578	43.4	5.4	−5.8	32970
47258.3965	0.109	32.6	5.8	−8.7	33220
47414.0776	0.033	38.2	5.0	−6.1	34212
47422.9379	0.142	33.9	5.2	−6.3	34267
47464.9085	0.661	51.3	5.6	−0.6	34633
47469.8194	0.722	53.0	9.8	0.1	3
47470.0047	0.724	49.0	9.4	−3.9	3
47470.8213	0.734	55.4	2.0	2.5	3
47471.0573	0.737	51.7	2.0	−1.2	3
47471.8378	0.747	56.1	2.0	3.2	3
47471.8404	0.747	54.9	1.5	1.9	3

Table 2—Continued

Date (HJD-2400000)	Orbital Phase	V_r (km s^{-1})	σ (km s^{-1})	$O-C$ (km s^{-1})	Source Code[a]
47473.0386	0.761	50.6	2.5	−2.4	3
47484.8542	0.907	40.2	6.9	−9.5	34770
47533.7509	0.512	45.1	5.6	−1.3	35282
47550.5978[b]	0.720	33.7	5.5	−19.1	35400
47556.6147	0.794	44.3	5.5	−8.4	35456
47560.6629	0.844	51.0	5.5	−0.7	3
47560.8172	0.846	50.6	5.7	−1.1	3
47561.6730	0.857	49.5	5.5	−2.0	3
47572.3104	0.988	31.8	5.0	−14.6	35551
47607.3133	0.421	34.0	5.0	−8.4	35833
47636.6277	0.783	42.4	5.6	−10.4	3
47636.6330	0.783	42.1	5.5	−10.8	3
47636.6381	0.783	43.9	5.4	−8.9	3
47638.6422	0.808	49.0	5.6	−3.5	3
47639.6267	0.820	48.3	5.8	−4.0	3
47640.6235	0.833	46.7	5.5	−5.4	3
47640.6276	0.833	47.5	5.4	−4.5	3
47789.9438	0.678	44.7	5.8	−7.5	37091
47871.8559	0.690	52.9	5.3	0.5	37795
47938.4644	0.514	45.4	4.8	−1.1	38198
47939.6030	0.528	42.5	11.8	−4.5	3
47940.7746	0.542	43.2	6.2	−4.5	3
47941.6557	0.553	42.7	8.1	−5.5	3
47941.6606	0.553	44.5	7.5	−3.6	3
47945.4140	0.600	55.1	5.2	5.1	38227
47981.7112	0.048	44.4	5.1	0.7	3
47983.6008	0.071	38.6	5.1	−4.1	3
48121.9663	0.782	57.4	4.3	4.5	3
48123.9556	0.806	55.0	8.7	2.5	3
48124.9817	0.819	47.3	1.5	−5.1	3
48125.0065	0.819	45.5	0.9	−6.8	3
48125.9833	0.831	55.7	2.7	3.6	3
48126.0140	0.832	55.8	2.3	3.7	3
48228.7021	0.101	46.5	5.1	4.9	40252
48230.6937	0.125	42.3	5.8	1.5	40271
48234.7019	0.175	48.0	6.3	8.5	40292
48313.6160	0.150	51.3	1.9	11.3	3
48318.5967	0.212	39.0	1.4	0.1	3
48318.6029	0.212	37.8	1.2	−1.1	3
48319.7591	0.226	37.4	1.7	−1.4	3
48320.6062	0.236	40.6	2.3	1.9	3
48320.6093	0.237	39.4	1.8	0.6	3
48321.6023	0.249	51.2	1.2	12.6	3
48351.4009	0.617	47.5	5.5	−3.1	41292
48353.4552	0.642	38.0	5.3	−13.4	41312

Table 2—Continued

Date (HJD-2400000)	Orbital Phase	V_r (km s^{-1})	σ (km s^{-1})	$O-C$ (km s^{-1})	Source Code[a]
48356.5255	0.680	49.6	5.2	−2.7	41329
48514.9599	0.638	58.0	4.7	6.7	3
48514.9619	0.639	55.5	2.9	4.2	3
48515.9288	0.650	53.6	4.2	2.0	3
48515.9315	0.650	54.2	3.9	2.5	3
48516.9660	0.663	61.1	6.1	9.1	3
49058.7301	0.359	47.9	1.4	7.6	3
49276.7565	0.053	46.4	5.5	2.9	48925
49335.5789	0.780	51.5	6.7	−1.3	49589
49374.4579	0.261	40.7	5.8	2.0	49862
49379.4985	0.323	37.4	4.8	−2.0	49900
49383.4999	0.373	32.6	5.8	−8.1	49918
49443.6959	0.117	42.1	3.5	1.1	3
49443.6977	0.117	42.8	2.2	1.7	3
49444.6856	0.129	43.0	0.8	2.4	3
49445.7002	0.141	43.0	1.2	2.7	3
49658.8770	0.776	45.0	5.7	−7.9	52713
49690.6816	0.169	39.1	4.9	−0.4	52974
49694.8170	0.220	36.3	6.3	−2.5	53010
49696.8457	0.245	41.9	6.0	3.2	53030
49783.5320	0.317	28.9	5.5	−10.4	54053
49816.5209	0.724	42.0	5.2	−10.8	54339
49976.9670	0.707	52.5	5.7	−0.2	55942
49976.9934	0.708	56.3	5.5	3.6	55943
50445.7157	0.501	44.4	1.1	−1.4	3
50446.7308	0.513	45.9	1.5	−0.5	3
50449.9064	0.552	46.4	1.9	−1.7	3
50449.9519	0.553	47.4	1.6	−0.8	3
50450.6275	0.561	47.1	1.0	−1.4	3
50451.6439	0.574	47.5	0.9	−1.6	3
51191.8840	0.722	56.3	0.6	3.5	3
51196.9206	0.785	53.8	0.9	1.0	3
51502.9245	0.566	51.7	1.8	3.0	3
51503.9888	0.580	52.2	0.7	3.0	3
51504.9810	0.592	53.1	0.6	3.4	3
51507.0622	0.618	52.5	0.6	1.9	3
51509.0572	0.642	52.0	0.9	0.6	3
51510.0615	0.655	53.2	0.9	1.5	3
51510.9336	0.665	54.9	0.7	2.9	3
51913.6433	0.643	48.4	0.5	−3.1	3
51914.6872	0.655	47.2	0.8	−4.5	3
51915.7806	0.669	46.6	0.8	−5.5	3
53291.9354	0.677	46.4	1.1	−5.9	4
53292.9944	0.690	46.4	1.0	−6.1	4
53294.9640	0.714	46.5	0.9	−6.3	4

Table 2—Continued

Date (HJD-2400000)	Orbital Phase	V_r (km s^{-1})	σ (km s^{-1})	$O-C$ (km s^{-1})	Source Code[a]
53294.9696	0.714	46.4	0.9	−6.3	4
54000.5828	0.435	34.6	8.2	−8.4	5
54020.9788	0.687	50.8	1.3	−1.7	4
54024.9341	0.736	46.8	1.3	−6.1	4
54041.5544	0.941	46.3	3.9	−2.1	5
54360.6253	0.885	49.1	6.3	−1.5	5
54365.6499	0.947	56.4	5.8	8.2	5
54366.6335	0.959	43.0	3.1	−4.6	5
54379.6041	0.119	36.5	3.2	−4.4	5
54387.5470	0.217	26.6	7.9	−12.3	5
54390.5816	0.255	38.1	3.7	−0.6	5
54396.5591	0.329	48.4	5.2	8.9	5
54405.5336	0.440	49.1	5.4	5.9	5
54468.3319	0.216	30.2	8.0	−8.6	5
54478.2873	0.339	22.8	18.2	−16.9	5
54504.2894	0.660	56.9	12.0	5.0	5
54506.3162	0.685	45.5	3.3	−6.9	5
54507.3105	0.697	54.6	7.7	2.0	5
54521.3459	0.871	40.5	5.2	−10.5	5
54527.4288	0.946	62.9	5.4	14.7	5
54555.3556	0.291	28.2	5.2	−10.7	5
54562.3347	0.377	31.9	33.3	−8.9	5
54563.3236	0.390	31.8	28.5	−9.5	5
54764.9840	0.882	44.9	0.6	−5.8	4
54774.0358	0.994	43.6	0.8	−2.5	4
54822.4689	0.592	48.3	8.9	−1.5	5
54879.3956	0.296	40.9	1.7	2.0	5
54887.4120	0.395	42.6	12.4	1.1	5
55576.4532	0.911	50.0	2.2	0.4	5
55988.3921	0.002	49.1	2.5	3.4	5
56000.3542	0.150	46.3	1.4	6.3	5
56271.5006	0.501	44.4	1.8	−1.4	5
56295.4159	0.796	50.0	3.9	−2.7	5
56630.1881	0.934	43.3	1.7	−5.4	5
56647.4494	0.147	43.7	2.5	3.6	5
56685.3676	0.616	51.6	1.6	1.0	5
56686.0369	0.624	45.9	1.7	−4.9	5
56711.3368	0.937	44.5	4.3	−4.1	5
56713.3043	0.961	44.0	2.9	−3.6	5
56733.6663	0.213	41.5	2.0	2.7	5
56739.3400	0.283	40.5	3.0	1.7	5
56741.5539	0.310	41.3	2.2	2.1	5
56745.6829	0.361	42.3	1.3	1.9	5
56998.7604	0.489	62.1	0.7	16.8	5
57042.6163	0.031	46.4	0.7	1.9	5

Table 2—Continued

Date (HJD-2400000)	Orbital Phase	V_r (km s^{-1})	σ (km s^{-1})	$O-C$ (km s^{-1})	Source Code[a]
57061.3817	0.263	45.6	2.1	6.9	5

[a]Source row listed in Table 1 or IUE SWP number if greater than 5.

[b]**This discrepant datum was** assigned zero-weight in orbital solution.

In order to combine the *IUE* and Hα measurements in a single orbital solution, we need to transform the relative *IUE* measurements to the frame of the Hα measurements. We did this by making preliminary orbital solutions to both sets, and then we applied the difference in the derived systemic velocity $\Delta\gamma = +28.68$ km s^{-1} to the *IUE* relative velocities, and these corrected velocities appear in Table 2. Likewise, we also wanted to include the original set of measurements of blue range spectroscopy from Peters (1983) in the final solution, so we again determined a systemic velocity difference $\Delta\gamma = +24.16$ km s^{-1} to place these measurements in the Hα frame. These adjusted measurements from Peters (1983) are also included in Table 2 for the convenience of the reader. **Neither shift should be interpreted in physical terms, but they are required to bring different kinds on measurements onto the same reference frame.**

We made an equally weighted fit of the radial velocities using the non-linear, least-squares method described by Morbey & Brosterhus (1974) to determine the spectroscopic orbital elements that are given in Table 3. We adopted a circular orbital solution because elliptical solutions made no significant improvement in the residuals from the fit. The elements are compared in Table 3 to those derived by Peters (1983), and the agreement is reasonable. The new period is somewhat larger (2.8σ different), and the uncertainty in the period is larger than given by Peters (1983). The new estimate of semiamplitude K_1 is slightly lower than found by Peters (1983) (2.2σ different). The radial velocities and orbital solution are shown in Figure 1, and we see that there is good agreement between the UV (larger scatter) and Hα results. We will use the new orbital elements throughout this paper with the epoch of phase zero, T_{sc}, defined as the time of superior conjunction of the Be star (as adopted by Peters 1983).

Table 3. Circular Orbital Elements

Element	This Study	Peters (1983)
P (days)	80.913 ± 0.018	80.860 ± 0.005
T_{sc} (HJD-2400000)	46845.0 ± 1.0	41990.5 ± 1.1
K_1 (km s^{-1})	7.1 ± 0.5	9.4 ± 0.9
γ(Hα) (km s^{-1})	45.8 ± 0.4	···
$f(m)$ ($M_\odot$)	0.0031 ± 0.0006	0.007 ± 0.002
$a_1 \sin\ i$ (10^6 km)	7.9 ± 0.5	10.4 ± 1.0
rms (km s^{-1})	5.8	4.1

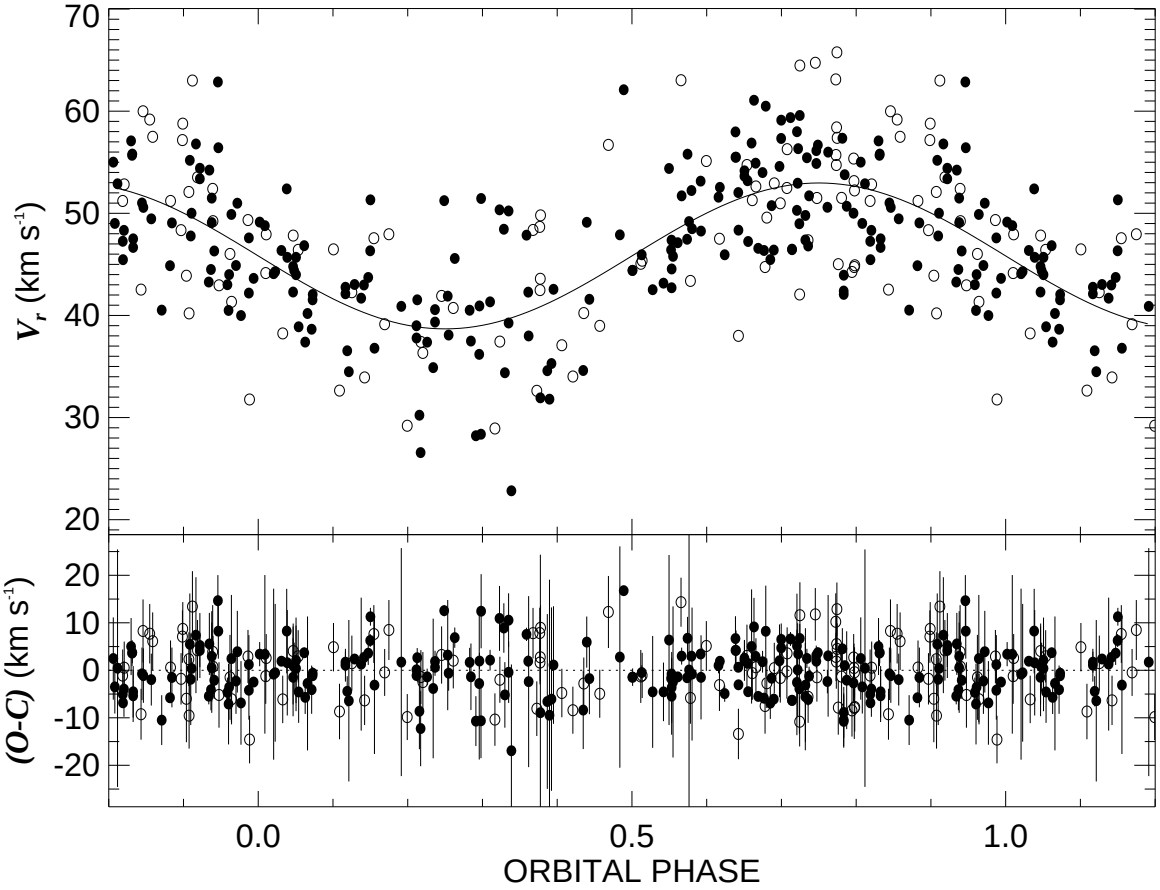

Fig. 1.— *Top panel:* Radial velocity curve for the Be star component of HR 2142. Orbital phase 0.0 corresponds to Be star superior conjunction. The solid circles represent the velocities from optical Hα spectroscopy and the open circles show the same from *IUE*. *Lower panel: the observed minus calculated residuals from the fit and their uncertainties.*

3. Detection of the FUV Flux of the Companion

We realized at the outset that the companion orbiting the Be star is probably too faint for direct detection of its lines in individual UV spectra because of the low S/N ($\approx$ 10) of the *IUE* spectra. Consequently, we adopted a search method based on cross-correlation techniques that was optimized for detection of a hot companion. First we selected a spectrum template from the non-LTE TLUSTY/SYNSPEC atmosphere models[4] of Lanz & Hubeny (2003) for $T_{\rm eff} \approx 45$ kK, $\log g = 4.75$ (the largest gravity value in the grid, but probably lower than actual), solar abundances, and no rotational broadening. Next, we restricted the wavelength range for the CCF to the far-UV, 1150 – 1189 Å (omitting the broad C III λ1176 feature of the Be star's spectrum), in order to focus on the part of the spectrum where the hot companion has a relatively larger flux contribution. Once the CCFs were calculated, we subtracted the mean CCF from each to remove any signal from correlation between the Be star's spectral features and those in the model template and to search for a component with the expected Doppler shifts of the companion.

Visual inspection of the individual difference CCFs did not immediately reveal any obvious signal from a hot companion. Thus, in the final step we shifted each of the difference CCFs to the **expected** Doppler reference frame of the companion, and then formed the mean of all the difference CCFs to seek the signal of the companion. We need to adopt a value of the mass ratio $q = M_2/M_1$ in order to estimate the Doppler shifts of the secondary star in each observation from the orbital radial velocity curve of the Be star (Table 3). We assumed a Be star mass of $10.5 M_\odot$ (appropriate for its spectral classification; Peters 2001) and then used the observed spectroscopic mass function $f(m) = (M_2 \sin i)^3/(M_1 + M_2)^2$ (Table 3) to determine the mass ratio q for a range in assumed orbital inclination i. The result ranges from $q = 0.077$ for $i = 65°$ to $q = 0.070$ for $i = 85°$, and we adopted the latter value based upon large inclination needed to account for the appearance of the shell features (see Section 4).

We show in Figure 2 the resulting CCF after shifting and averaging all 88 individual difference CCFs formed using the hot model spectrum as a template. We find that there is indeed a peak near the expected rest frame zero velocity that corresponds to correlation with the weak spectral features of the companion. The peak reaches a maximum that is 4σ above the background, so we suggest that this approach offers us the first tentative detection of the spectrum of the hot companion.

Figure 2 also shows a Gaussian fit of the peak with parameters of peak height $p =$

[4]http://nova.astro.umd.edu/

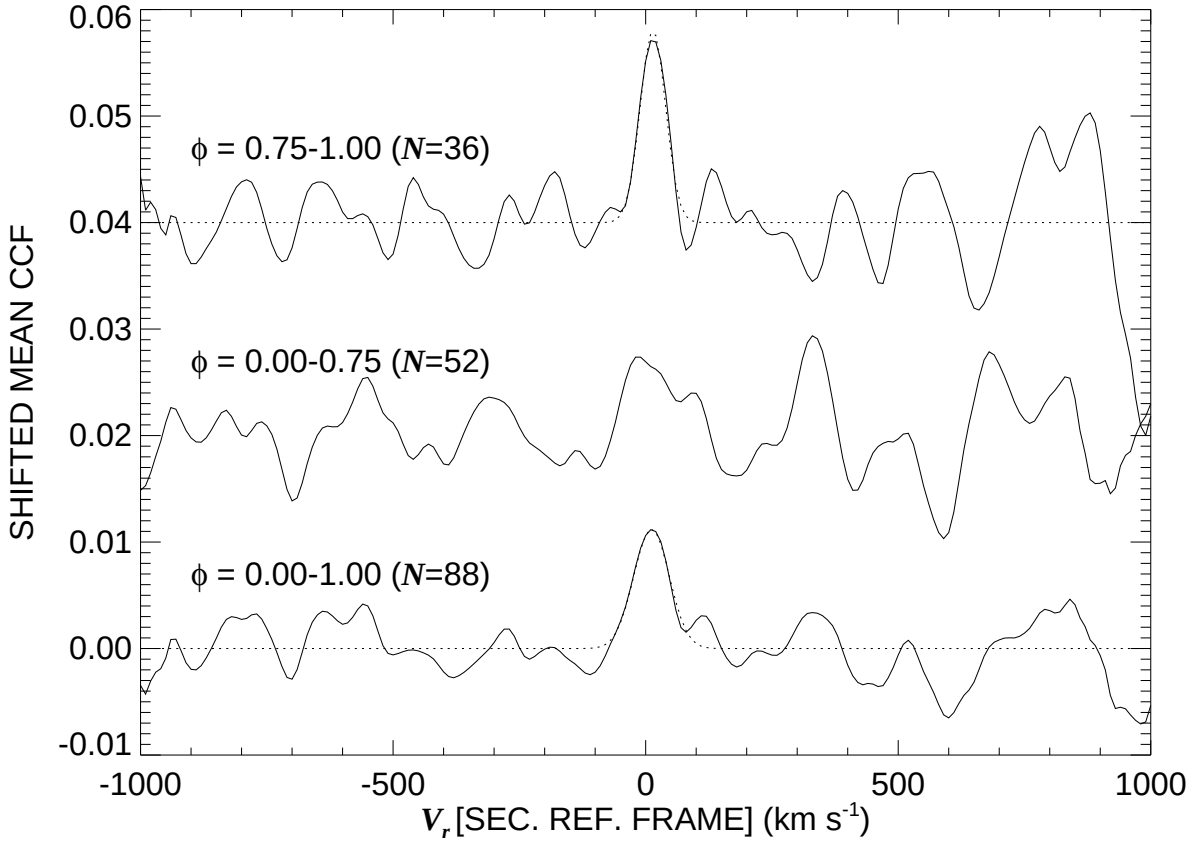

Fig. 2.— The lower plot shows the mean CCF of the FUV spectra (1150–1189 Å) with a hot model spectrum after subtraction of the overall mean CCF and shifting each to the adopted reference frame of the faint secondary. A Gaussian fit of the weak central peak is shown as a dotted line. The middle and upper plots show the same for subsamples from orbital phases $\phi = 0.00 - 0.75$ and $0.75 - 1.00$ offset by +0.02 and +0.04, respectively, with the number of spectra N noted in the label. The much weaker signal in the phase range $\phi = 0.00 - 0.75$ suggests phase-variable obscuration of the secondary spectrum.

0.0112 ± 0.0012, a central position of $V_r = 12 \pm 5$ km s^{-1}, and a Gaussian dispersion of $\sigma = 35 \pm 5$ km s^{-1}. We think the small velocity offset is insignificant (probably resulting from model mis-match and uncertainties in the physical value of the systemic velocity), and the dispersion σ is that expected from cross-correlations of model spectra with no rotational broadening. Thus, if we accept the detection as reliable, then the projected rotational velocity of the companion must be small, $V \sin i < 30$ km s^{-1}.

We experimented with using a range in assumed model $T_{\rm eff}$ and mass ratio $q = M_2/M_1$ to find values that maximized the peak height of the CCF signal. We took the uncertainty associated with the Gaussian fit of the peak height to find the range over which the resulting peak height exceeded $p(\max) - 1\sigma = 0.010$. The optimal results are $T_{\rm eff} = 43 \pm 5$ kK and $q = 0.072 \pm 0.021$. The derived mass ratio q agrees with our estimate from the mass function (based upon $f(m)$, M_1, i). We caution that the $T_{\rm eff}$ estimate is probably a lower limit, because the model template was based on a smaller than actual $\log g$ and the ionization balance reflected in the relative line strengths will lead to higher temperature at higher gravity.

Figure 2 also shows the results of restricting the sample according to orbital phase. We found that the peak is weak or absent in the difference CCFs from orbital phases $\phi = 0.00$ to 0.75 (middle plot) but is relatively stronger in the range $\phi = 0.75$ to 1.00 (upper plot), i.e., between the times of fastest secondary approach and secondary inferior conjunction. This is suggestive of phase-variable obscuration of the flux of the hot companion (perhaps due to circumstellar gas structures; see the discussion in Section 5). Because some obscuration may also be present in the phase range $\phi = 0.75$ to 1.00, we will assume that the peak height $p = 0.0180 \pm 0.0023$ observed then represents a lower limit to the signal from the flux contribution of the hot secondary star.

Finally, we made a sequence of model difference CCFs using the mean spectrum to represent that of the Be star and the optimum model template for the secondary, and the flux contributions of both stars were summed for a grid of assumed values of flux ratio f_2/f_1. We measured the height of the resulting peak in the difference CCF to form a linear relation between f_2/f_1 and p. This relationship leads to a monochromatic flux ratio estimate of $f_2/f_1 > 0.0088 \pm 0.0011$ in the region from 1150 to 1189 Å, i.e., the companion contributes at least 0.9% of the flux in this spectral range.

The observed flux ratio is approximately related to radius ratio by

$$\frac{f_2}{f_1} = \frac{F_2}{F_1} \left(\frac{R_2}{R_1} \right)^2 \tag{1}$$

where F_2/F_1 is the monochromatic flux ratio per unit area. Using adopted temperatures of

21 kK and 43 kK for the Be star and companion, respectively, we estimate that $F_2/F_1 = 12.8$ at 1170 Å based upon the TLUSTY/SYNSPEC models. Then the radius ratio is $R_2/R_1 > 0.026 \pm 0.002$, and if we assume $R_1 = 5R_\odot$ based upon the spectral classification of the Be star, then the companion radius is $R_2 > 0.13R_\odot$.

4. Orbital Variations of Shell Lines

The shell absorption features that appear each orbit in the spectrum of HR 2142 may originate in disk structures created by the gravity of the companion (Section 5), so it is important to document the appearance and orbital variability of these shell components. The optical spectral variations of the shell lines were described by Peters (1983), and they begin about six days prior to Be star superior conjunction displaying red-shifts in a *primary shell phase*, and this is followed by a short 1.5 day *secondary shell phase* of blue-shifted absorption immediately after the time of conjunction. The UV spectrum is rich in similar shell line features, and in this section we present plots of orbital variations in the strongest of the observed shell features.

Figure Set 3 (given in full in the electronic edition) documents the shell line variations for 18 representative and strong absorption features. Rest wavelengths are derived from Morton et al. (1988) or the NIST database[5]. The top panel of each figure consists of line plots offset in flux according to the orbital phase of observation, and the lower panel shows the same set of spectra represented as a gray scale image of spectral flux strength as a function of Doppler shift and orbital phase. Many of these features also display a radial velocity constant component that is formed in the interstellar medium and/or Be disk. Thus, it is informative to begin the discussion with a representative case where the constant component is absent. An excellent example is the Si II λ1264 line that is shown in Figure 3.5. Here the shell feature begins near $V_r = 0$ km s^{-1} shortly after orbital phase $\phi = 0.5$ (Be star inferior conjunction), and it becomes wider and deeper to reach maximum absorption just before $\phi = 0.0$. Then the red-shifted absorption abruptly disappears and a short-lived blue-shifted component is briefly seen. These two manifestations are the UV counterparts of the *primary* and *secondary shell phases* seen in optical spectral lines (Peters 1983). The absorption maximum during the *primary shell phase* occurs near $\phi = 0.95$ and spans a velocity range of +10 to +160 km s^{-1}. The *secondary shell phase* occurs near $\phi = 0.03$ and spans a velocity range of −40 to +20 km s^{-1}. This basic pattern of variation is repeated in many other lines including Si II λ1193 (Fig. 3.1), Si III λ1299 (Fig. 3.6), and S III λ1200 (Fig. 3.2).

[5]http://physics.nist.gov/cgi-bin/ASD/lines1.pl

Fig. Set 3. Shell Line Variations

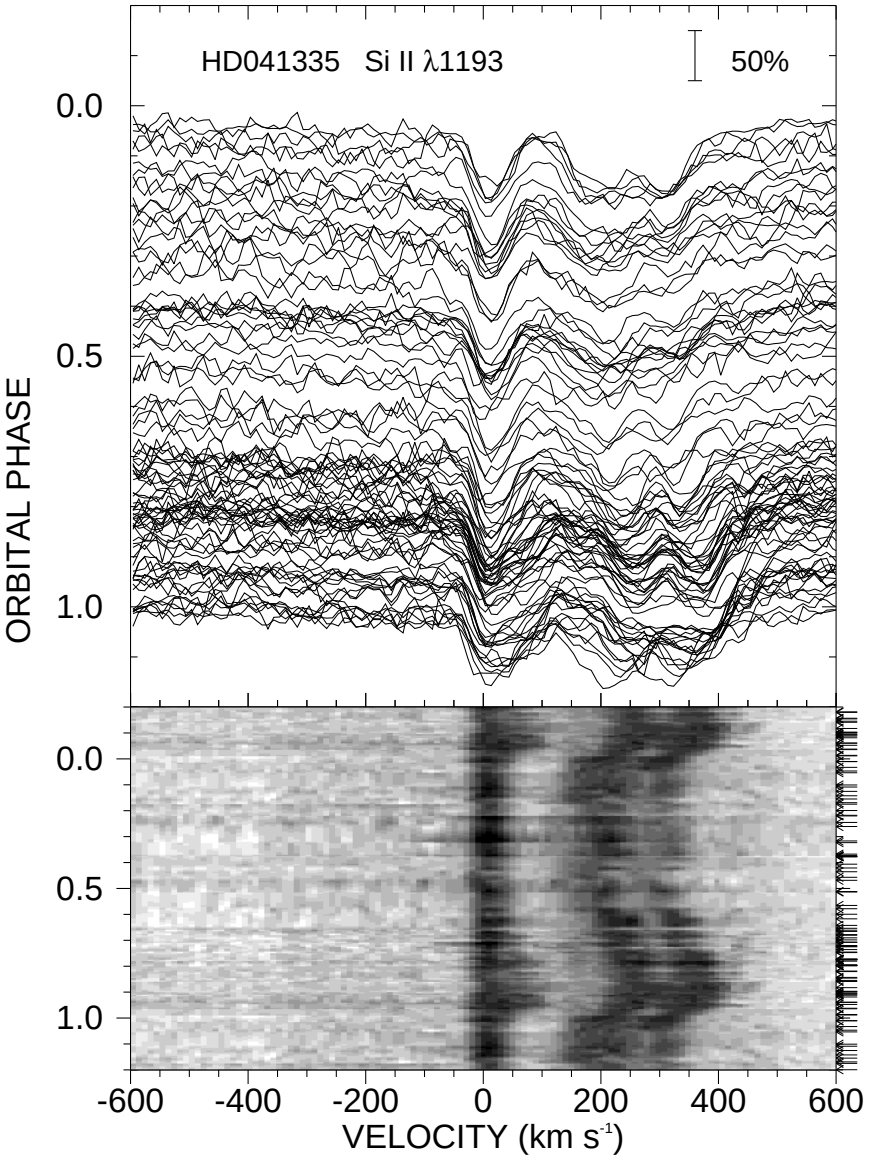

Fig. 3.1.— The top panel shows the individual spectra of Si II λ1193.290 plotted as a function of radial velocity and orbital phase (such that the continuum is aligned with the phase of observation). The spectral flux depth relative to the continuum is indicated by the scale bar in upper right. The lower panel shows the same interpolated in orbital phase and portrayed as a gray scale image (black corresponding to deepest absorption and white to strongest continuum flux). The actual phases of observation are indicated by arrows on the right hand side. The lines of S III $\lambda\lambda$1194.061, 1194.457 appear offset to higher velocity.

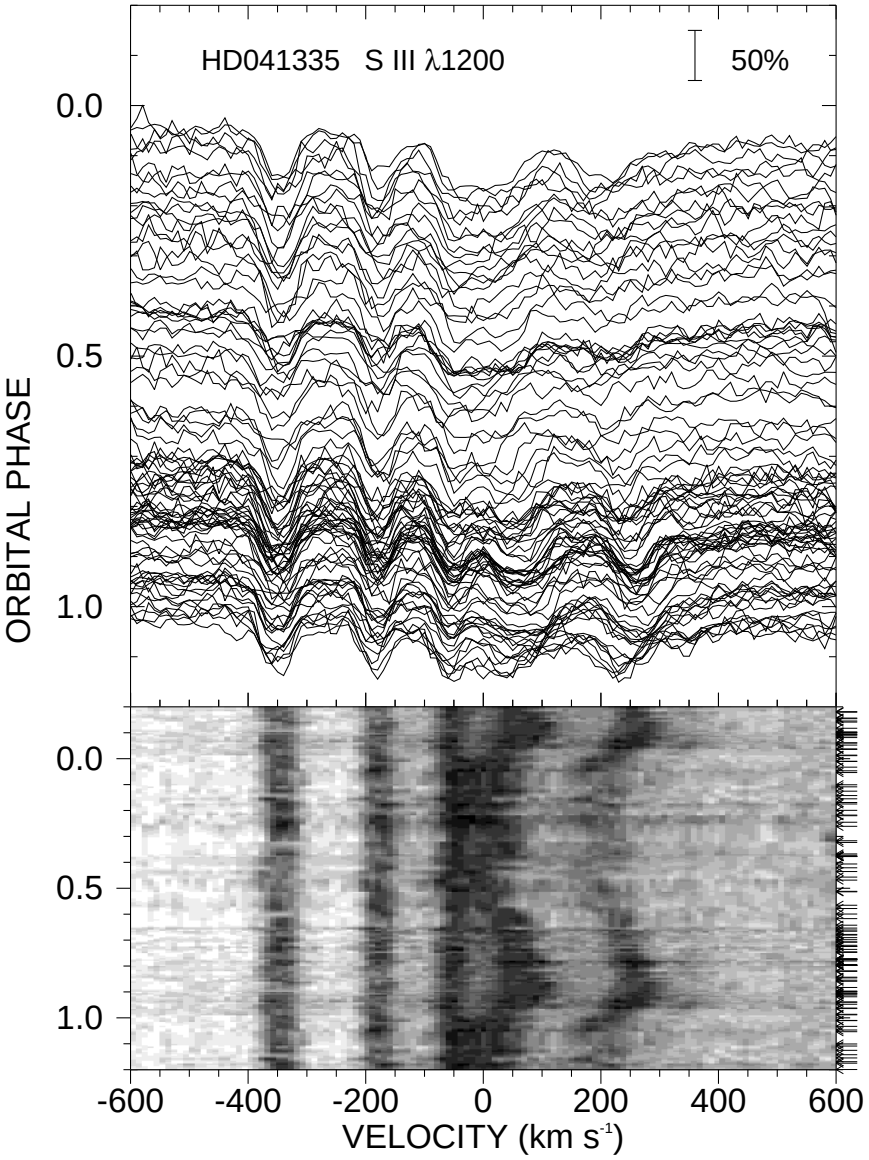

Fig. 3.2.— The top panel shows the individual spectra of S III λ1200.970 plotted as a function of radial velocity and orbital phase (such that the continuum is aligned with the phase of observation). The spectral flux depth relative to the continuum is indicated by the scale bar in upper right. The lower panel shows the same interpolated in orbital phase and portrayed as a gray scale image (black corresponding to deepest absorption and white to strongest continuum flux). The actual phases of observation are indicated by arrows on the right hand side. The stationary lines of N I $\lambda\lambda$1199.5, 1200.2, 1200.7 appear offset to lower velocity, while S III λ1201.730 appears at higher velocity.

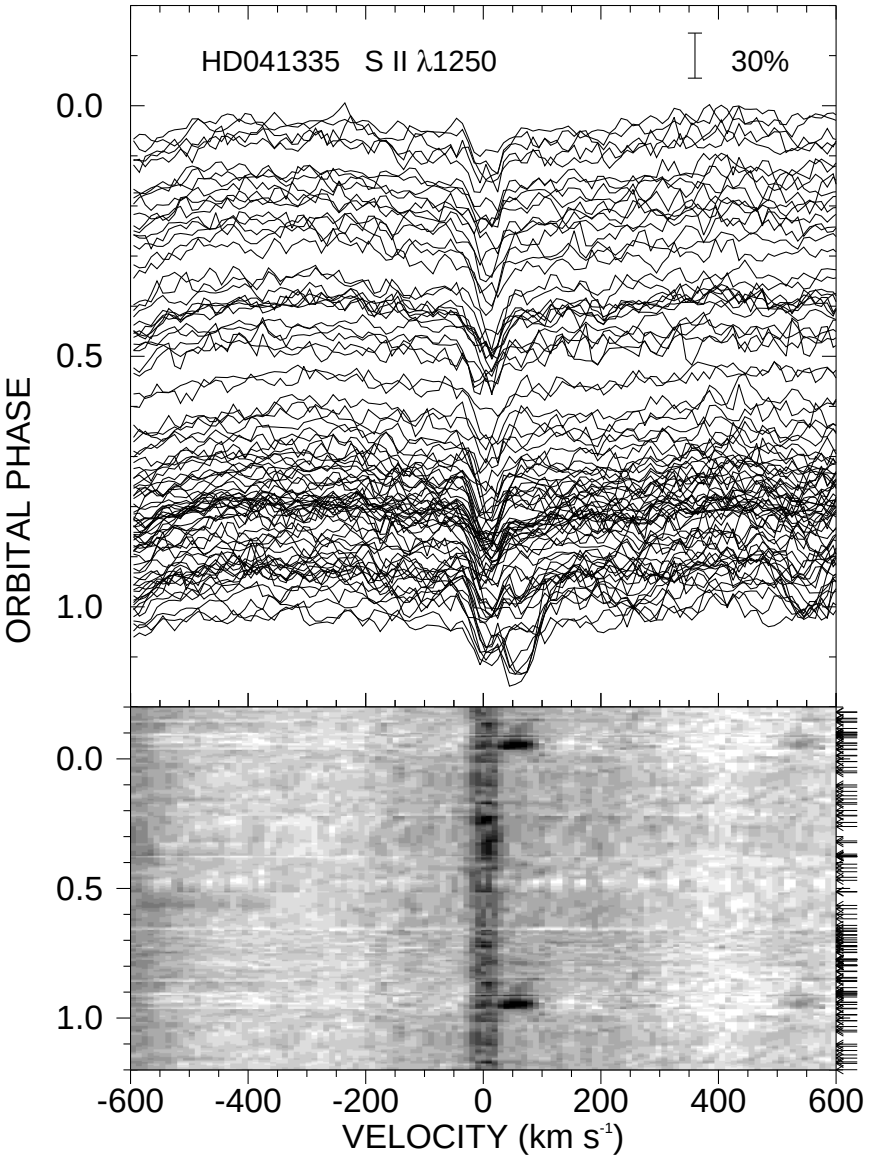

Fig. 3.3.— The top panel shows the individual spectra of S II λ1250.583 plotted as a function of radial velocity and orbital phase (such that the continuum is aligned with the phase of observation). The spectral flux depth relative to the continuum is indicated by the scale bar in upper right. The lower panel shows the same interpolated in orbital phase and portrayed as a gray scale image (black corresponding to deepest absorption and white to strongest continuum flux). The actual phases of observation are indicated by arrows on the right hand side. The shell line is visible only close to orbital phase $\phi = 0.95$.

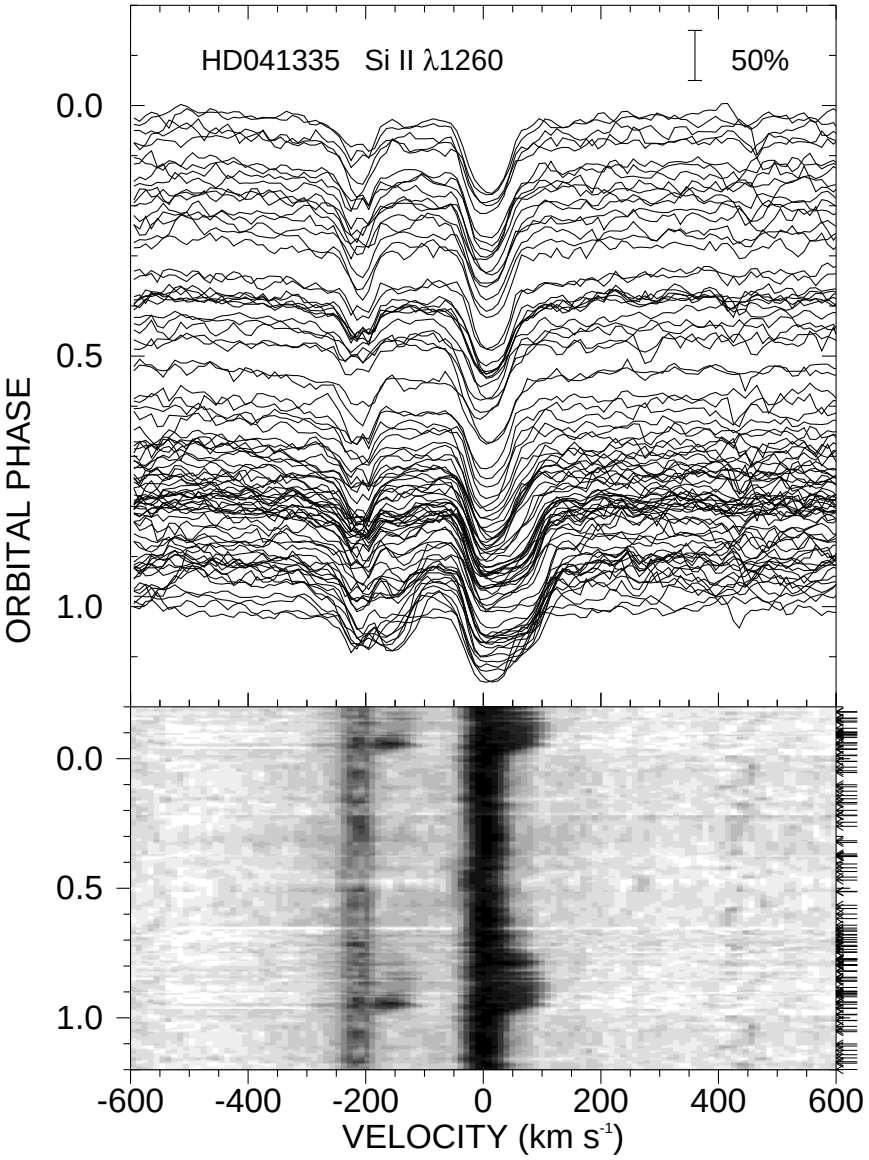

Fig. 3.4.— The top panel shows the individual spectra of Si II λ1260.4223 plotted as a function of radial velocity and orbital phase (such that the continuum is aligned with the phase of observation). The spectral flux depth relative to the continuum is indicated by the scale bar in upper right. The lower panel shows the same interpolated in orbital phase and portrayed as a gray scale image (black corresponding to deepest absorption and white to strongest continuum flux). The actual phases of observation are indicated by arrows on the right hand side. The shell component of S II λ1259.518 (offset to lower velocity) is visible only close to orbital phase $\phi = 0.95$.

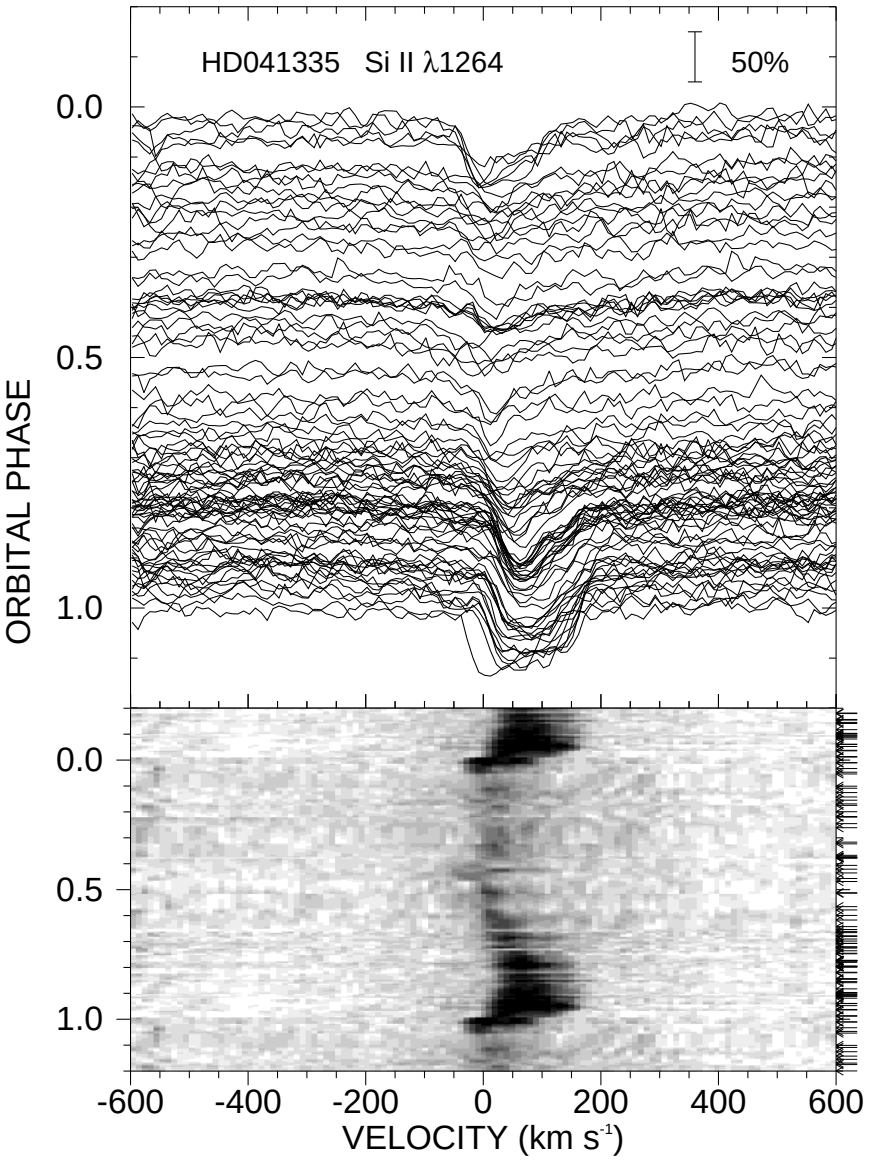

Fig. 3.5.— The top panel shows the individual spectra of Si II λ1264.73 plotted as a function of radial velocity and orbital phase (such that the continuum is aligned with the phase of observation). The spectral flux depth relative to the continuum is indicated by the scale bar in upper right. The lower panel shows the same interpolated in orbital phase and portrayed as a gray scale image (black corresponding to deepest absorption and white to strongest continuum flux). The actual phases of observation are indicated by arrows on the right hand side.

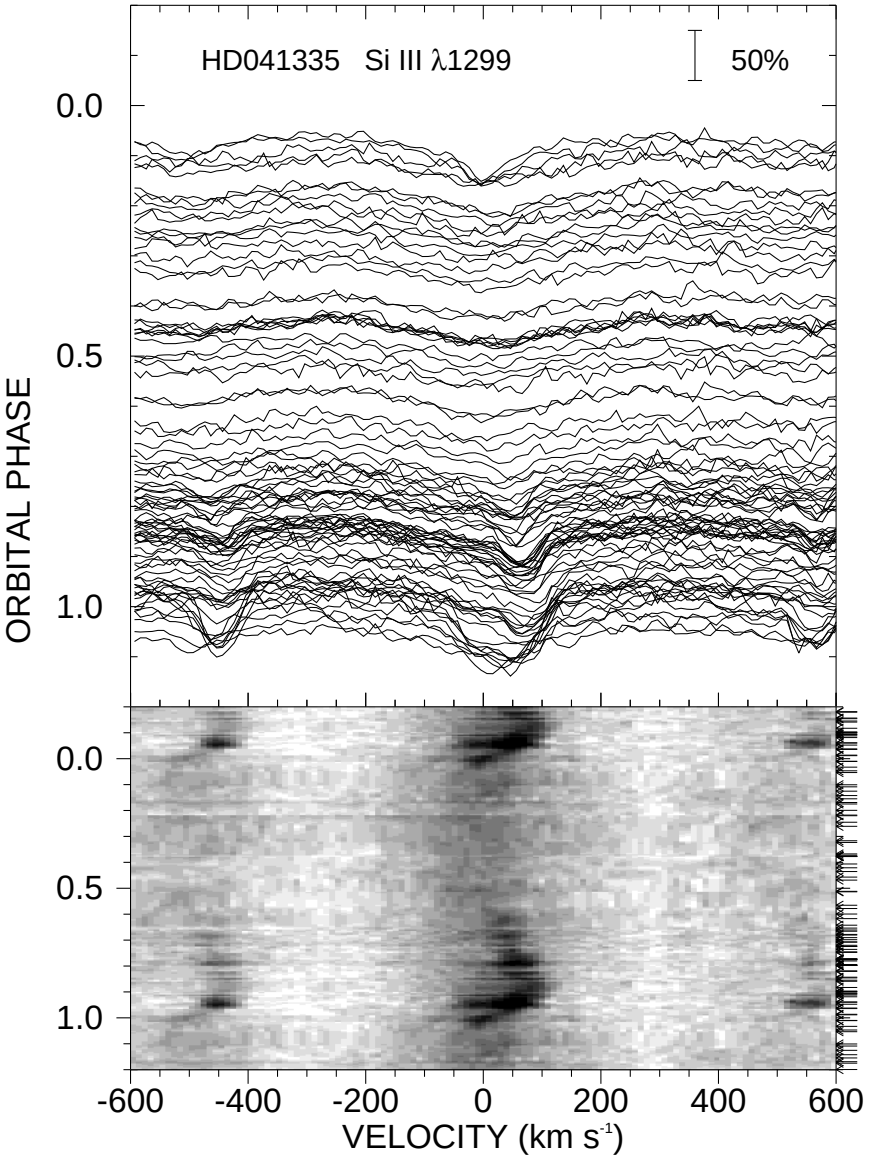

Fig. 3.6.— The top panel shows the individual spectra of Si III λ1298.96 plotted as a function of radial velocity and orbital phase (such that the continuum is aligned with the phase of observation). The spectral flux depth relative to the continuum is indicated by the scale bar in upper right. The lower panel shows the same interpolated in orbital phase and portrayed as a gray scale image (black corresponding to deepest absorption and white to strongest continuum flux). The actual phases of observation are indicated by arrows on the right hand side. The lines of Si III $\lambda\lambda$1296.73, 1298.89, 1301.15 also appear as sudden shell features at orbital phase $\phi = 0.95$.

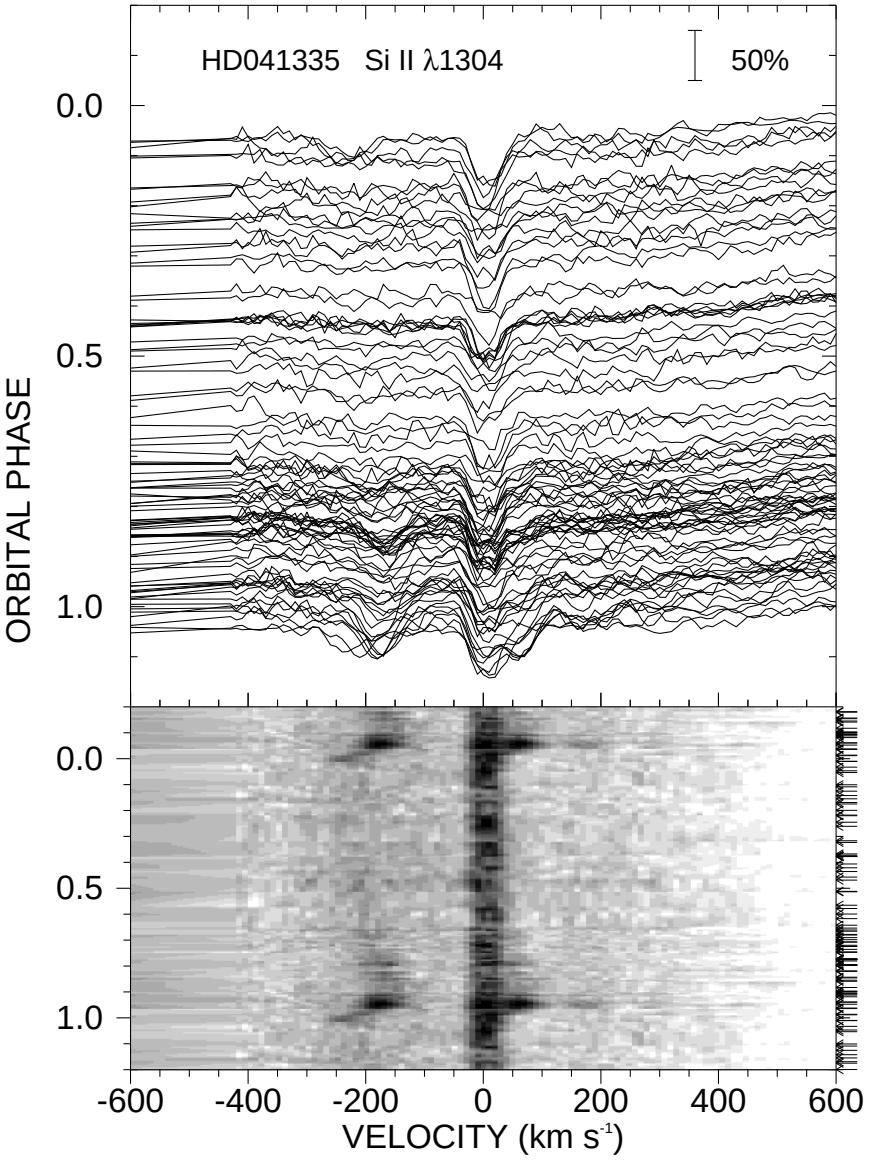

Fig. 3.7.— The top panel shows the individual spectra of Si II λ1304.3711 plotted as a function of radial velocity and orbital phase (such that the continuum is aligned with the phase of observation). The spectral flux depth relative to the continuum is indicated by the scale bar in upper right. The lower panel shows the same interpolated in orbital phase and portrayed as a gray scale image (black corresponding to deepest absorption and white to strongest continuum flux). The actual phases of observation are indicated by arrows on the right hand side. The shell component appears suddenly at orbital phase $\phi = 0.95$. The flat region at left represents a linear interpolation across the interstellar line of O I λ1302.

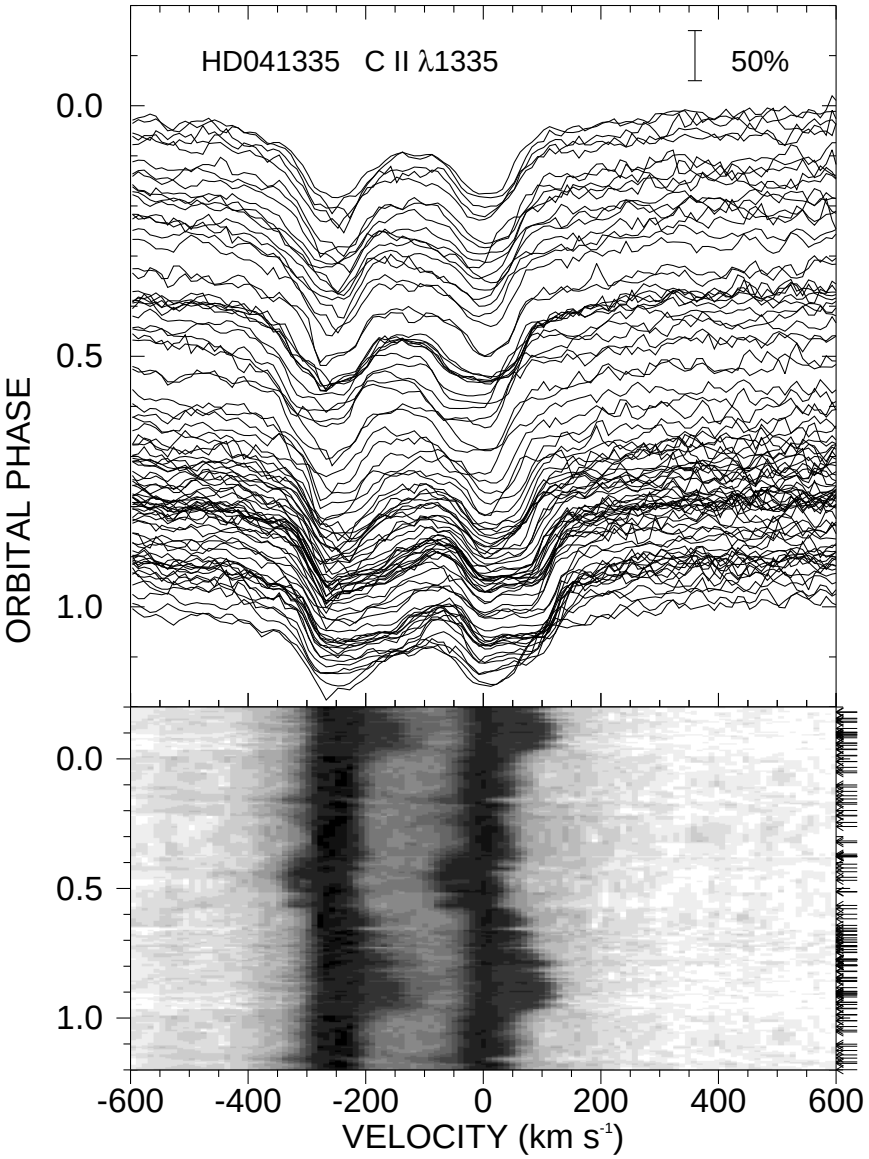

Fig. 3.8.— The top panel shows the individual spectra of C II λ1335.708 plotted as a function of radial velocity and orbital phase (such that the continuum is aligned with the phase of observation). The spectral flux depth relative to the continuum is indicated by the scale bar in upper right. The lower panel shows the same interpolated in orbital phase and portrayed as a gray scale image (black corresponding to deepest absorption and white to strongest continuum flux). The actual phases of observation are indicated by arrows on the right hand side. The similar line of C II λ1334.532 appears offset to lower velocity.

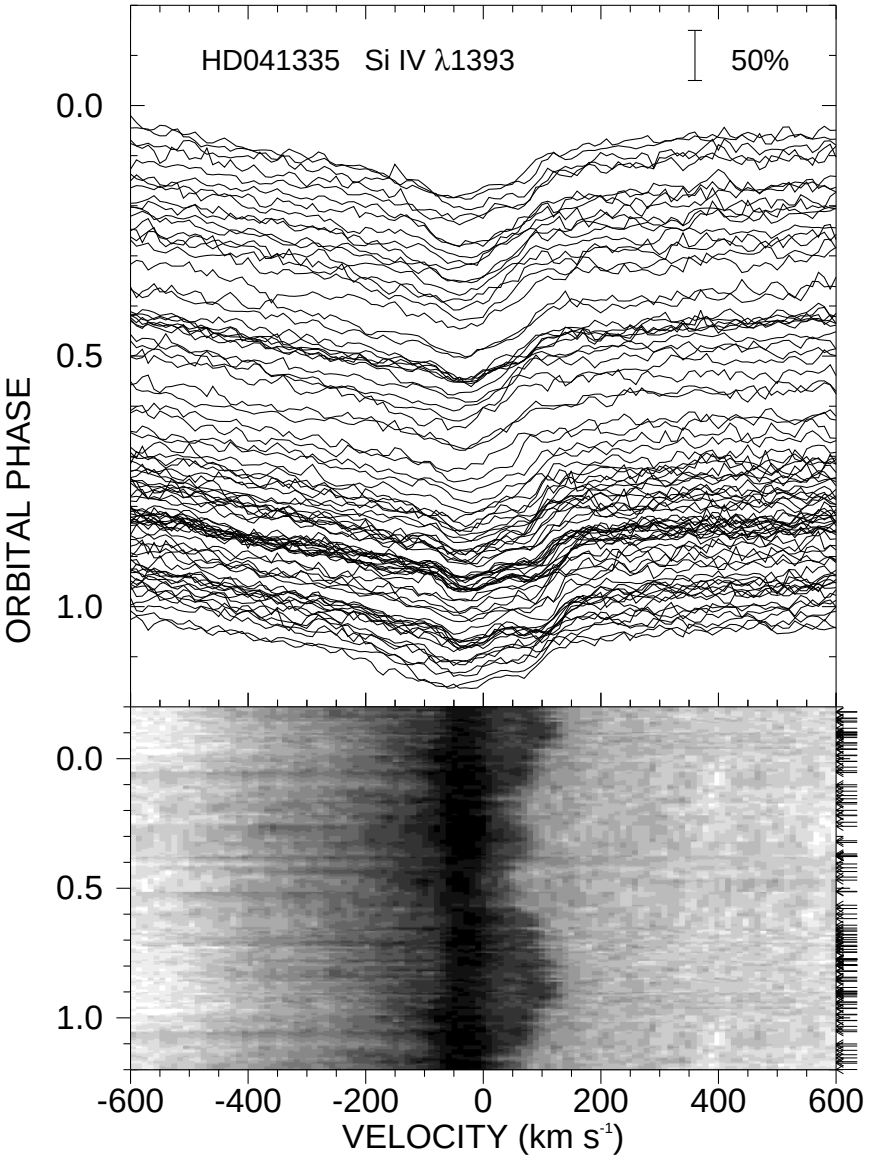

Fig. 3.9.— The top panel shows the individual spectra of Si IV λ1393.755 plotted as a function of radial velocity and orbital phase (such that the continuum is aligned with the phase of observation). The spectral flux depth relative to the continuum is indicated by the scale bar in upper right. The lower panel shows the same interpolated in orbital phase and portrayed as a gray scale image (black corresponding to deepest absorption and white to strongest continuum flux). The actual phases of observation are indicated by arrows on the right hand side. The feature is formed mainly in the wind of the Be star, but shell variations are present on the high velocity side of the core.

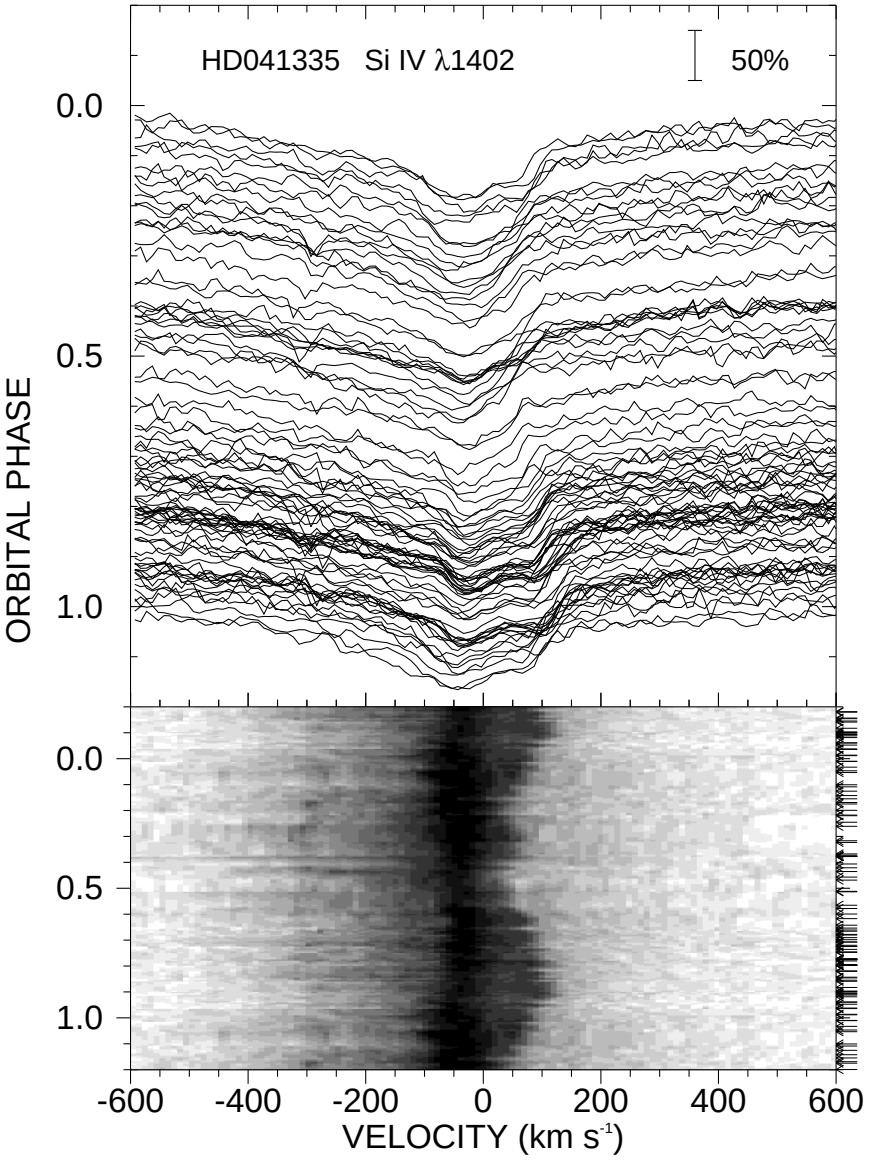

Fig. 3.10.— The top panel shows the individual spectra of Si IV λ1402.770 plotted as a function of radial velocity and orbital phase (such that the continuum is aligned with the phase of observation). The spectral flux depth relative to the continuum is indicated by the scale bar in upper right. The lower panel shows the same interpolated in orbital phase and portrayed as a gray scale image (black corresponding to deepest absorption and white to strongest continuum flux). The actual phases of observation are indicated by arrows on the right hand side. The feature is formed mainly in the wind of the Be star, but shell variations are present on the high velocity side of the core.

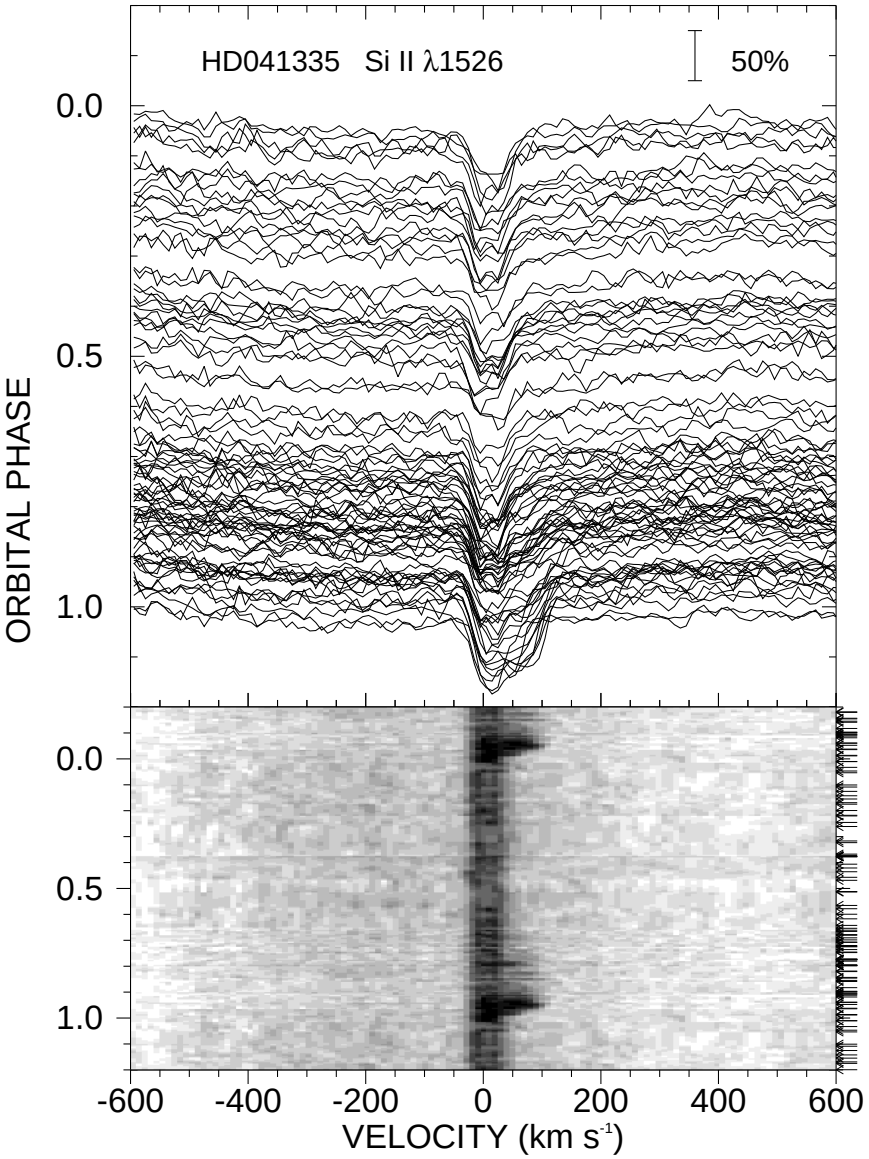

Fig. 3.11.— The top panel shows the individual spectra of Si II λ1526.7071 plotted as a function of radial velocity and orbital phase (such that the continuum is aligned with the phase of observation). The spectral flux depth relative to the continuum is indicated by the scale bar in upper right. The lower panel shows the same interpolated in orbital phase and portrayed as a gray scale image (black corresponding to deepest absorption and white to strongest continuum flux). The actual phases of observation are indicated by arrows on the right hand side. The shell component appears suddenly at orbital phase $\phi = 0.95$.

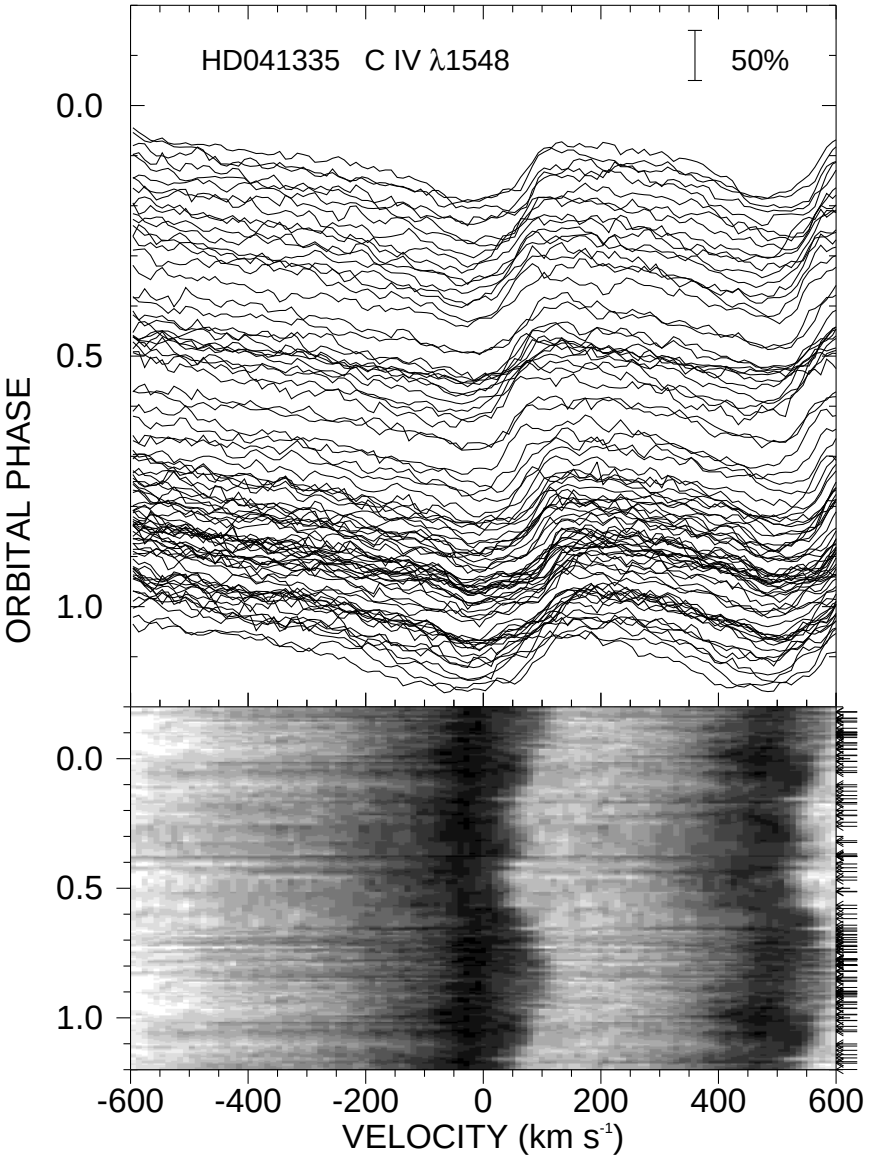

Fig. 3.12.— The top panel shows the individual spectra of C IV λ1548.202 plotted as a function of radial velocity and orbital phase (such that the continuum is aligned with the phase of observation). The spectral flux depth relative to the continuum is indicated by the scale bar in upper right. The lower panel shows the same interpolated in orbital phase and portrayed as a gray scale image (black corresponding to deepest absorption and white to strongest continuum flux). The actual phases of observation are indicated by arrows on the right hand side. The similar line of C IV λ1550.774 appears offset to higher velocity. Both features are formed mainly in the wind of the Be star, but shell variations are present on the high velocity side of the core.

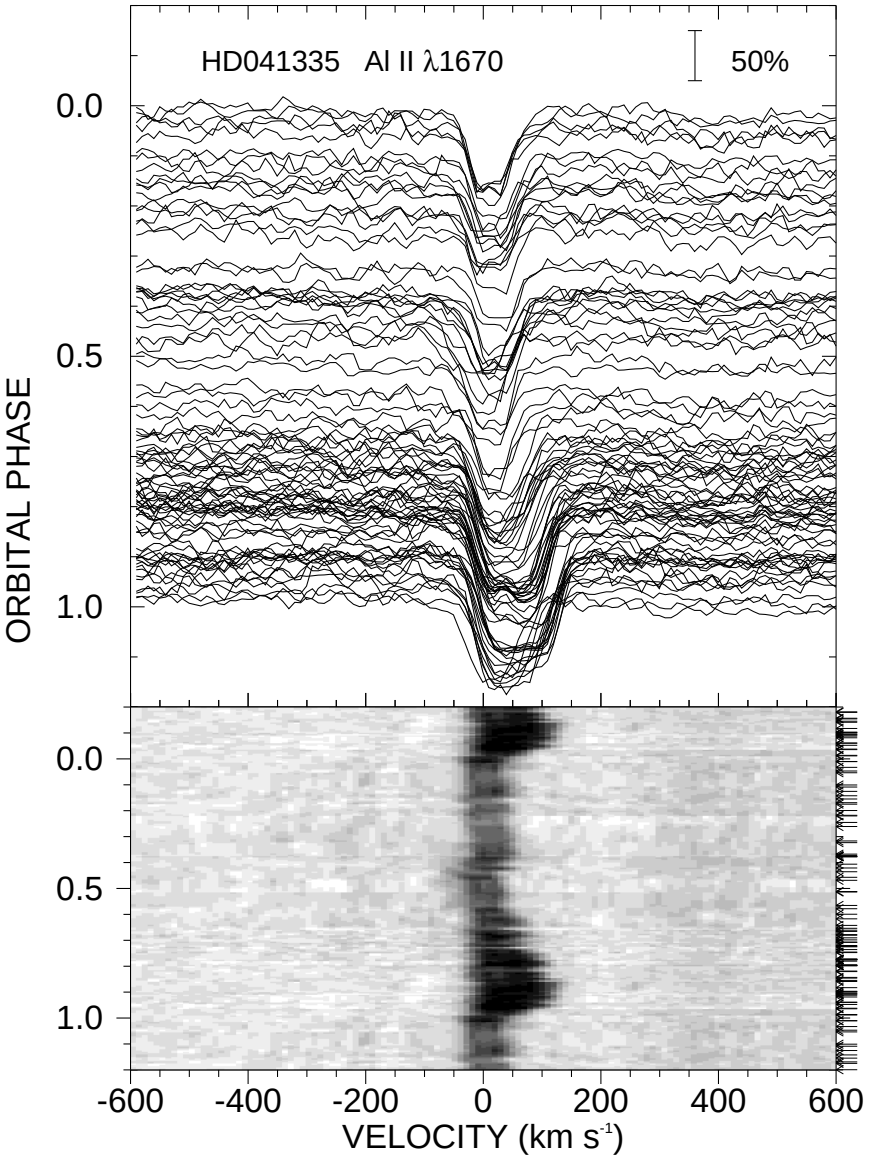

Fig. 3.13.— The top panel shows the individual spectra of Al II λ1670.7867 plotted as a function of radial velocity and orbital phase (such that the continuum is aligned with the phase of observation). The spectral flux depth relative to the continuum is indicated by the scale bar in upper right. The lower panel shows the same interpolated in orbital phase and portrayed as a gray scale image (black corresponding to deepest absorption and white to strongest continuum flux). The actual phases of observation are indicated by arrows on the right hand side.

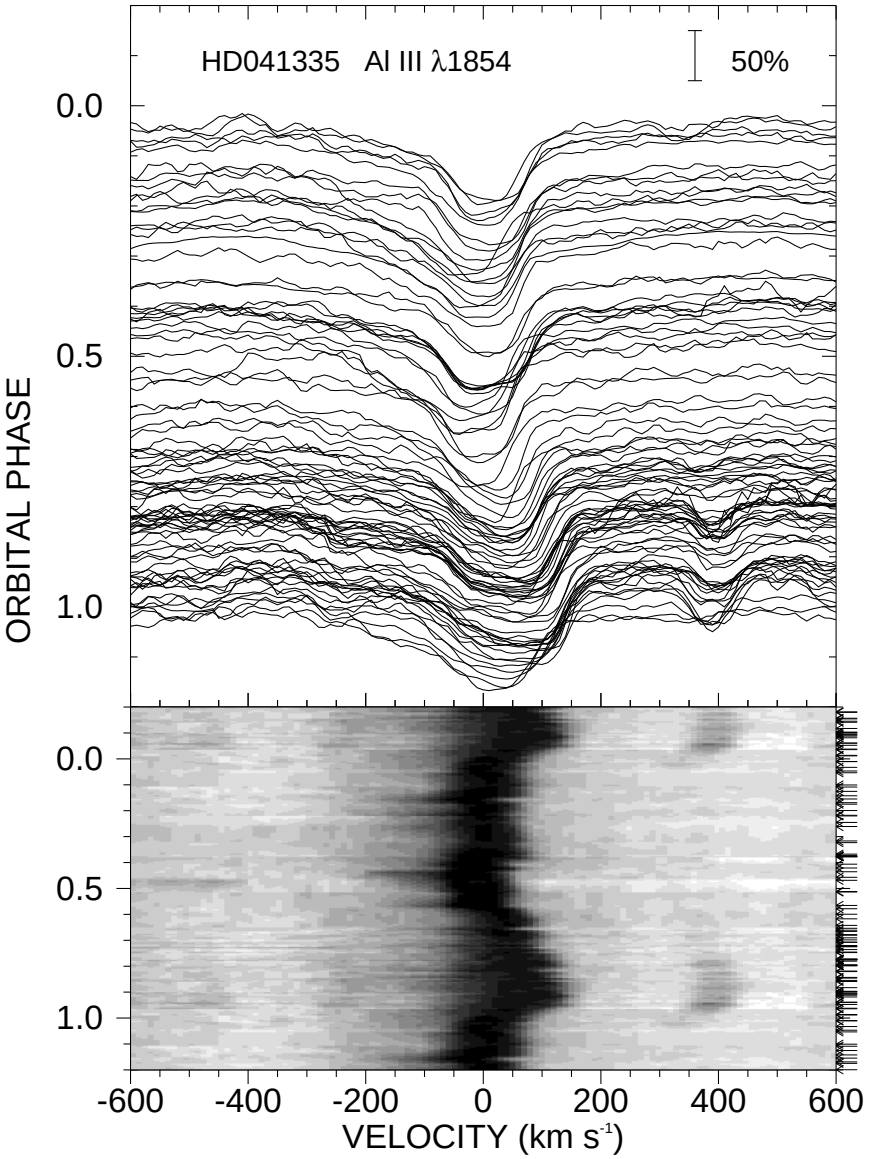

Fig. 3.14.— The top panel shows the individual spectra of Al III λ1854.7164 plotted as a function of radial velocity and orbital phase (such that the continuum is aligned with the phase of observation). The spectral flux depth relative to the continuum is indicated by the scale bar in upper right. The lower panel shows the same interpolated in orbital phase and portrayed as a gray scale image (black corresponding to deepest absorption and white to strongest continuum flux). The actual phases of observation are indicated by arrows on the right hand side.

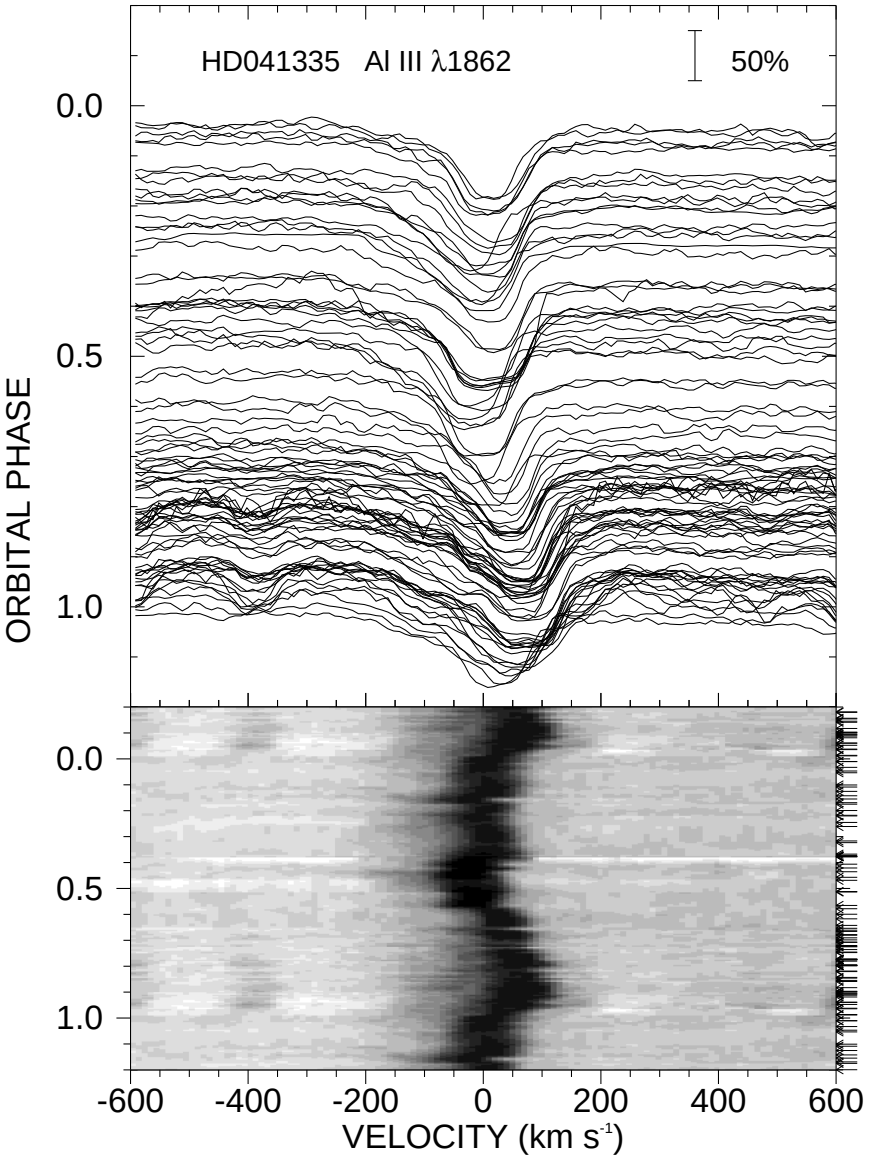

Fig. 3.15.— The top panel shows the individual spectra of Al III λ1862.7895 plotted as a function of radial velocity and orbital phase (such that the continuum is aligned with the phase of observation). The spectral flux depth relative to the continuum is indicated by the scale bar in upper right. The lower panel shows the same interpolated in orbital phase and portrayed as a gray scale image (black corresponding to deepest absorption and white to strongest continuum flux). The actual phases of observation are indicated by arrows on the right hand side.

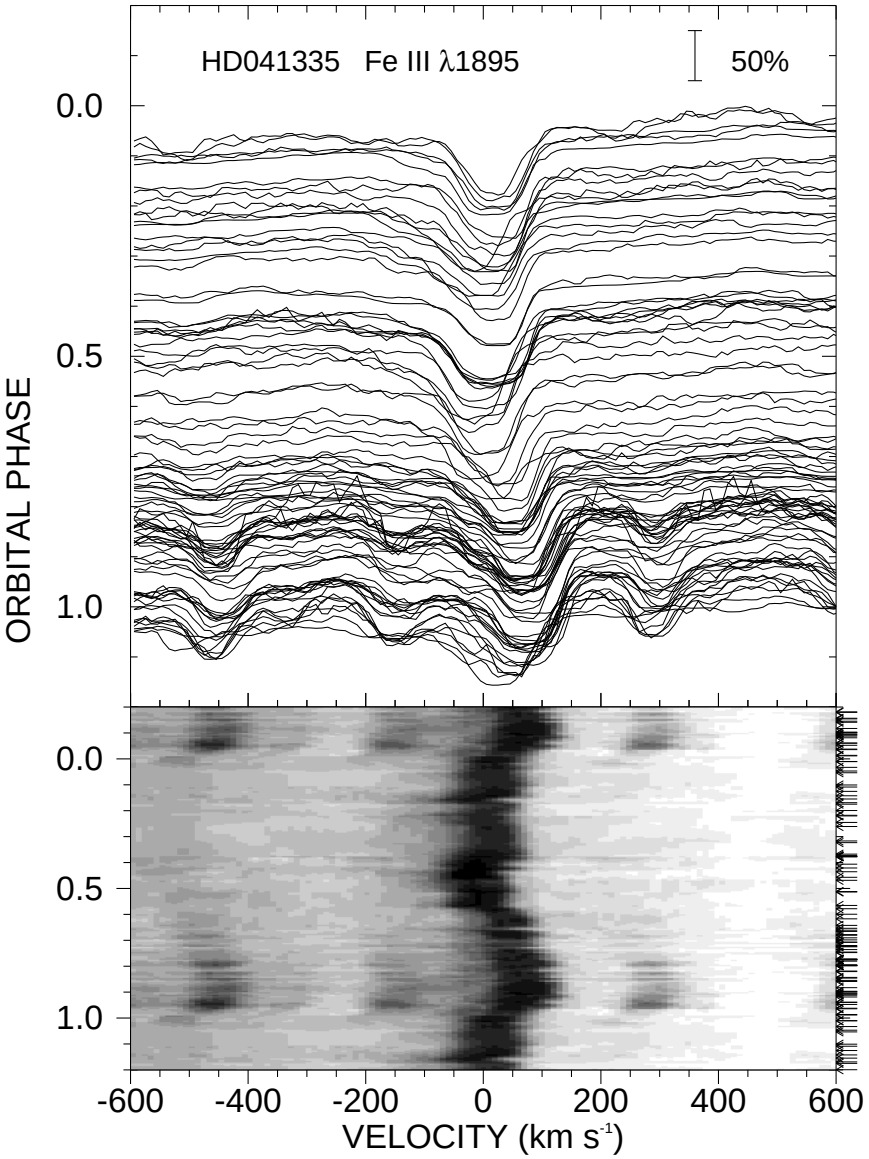

Fig. 3.16.— The top panel shows the individual spectra of Fe III λ1895.46 plotted as a function of radial velocity and orbital phase (such that the continuum is aligned with the phase of observation). The spectral flux depth relative to the continuum is indicated by the scale bar in upper right. The lower panel shows the same interpolated in orbital phase and portrayed as a gray scale image (black corresponding to deepest absorption and white to strongest continuum flux). The actual phases of observation are indicated by arrows on the right hand side. The lines of Fe III $\lambda\lambda$1895.46, 1896.814 also appear in the figure.

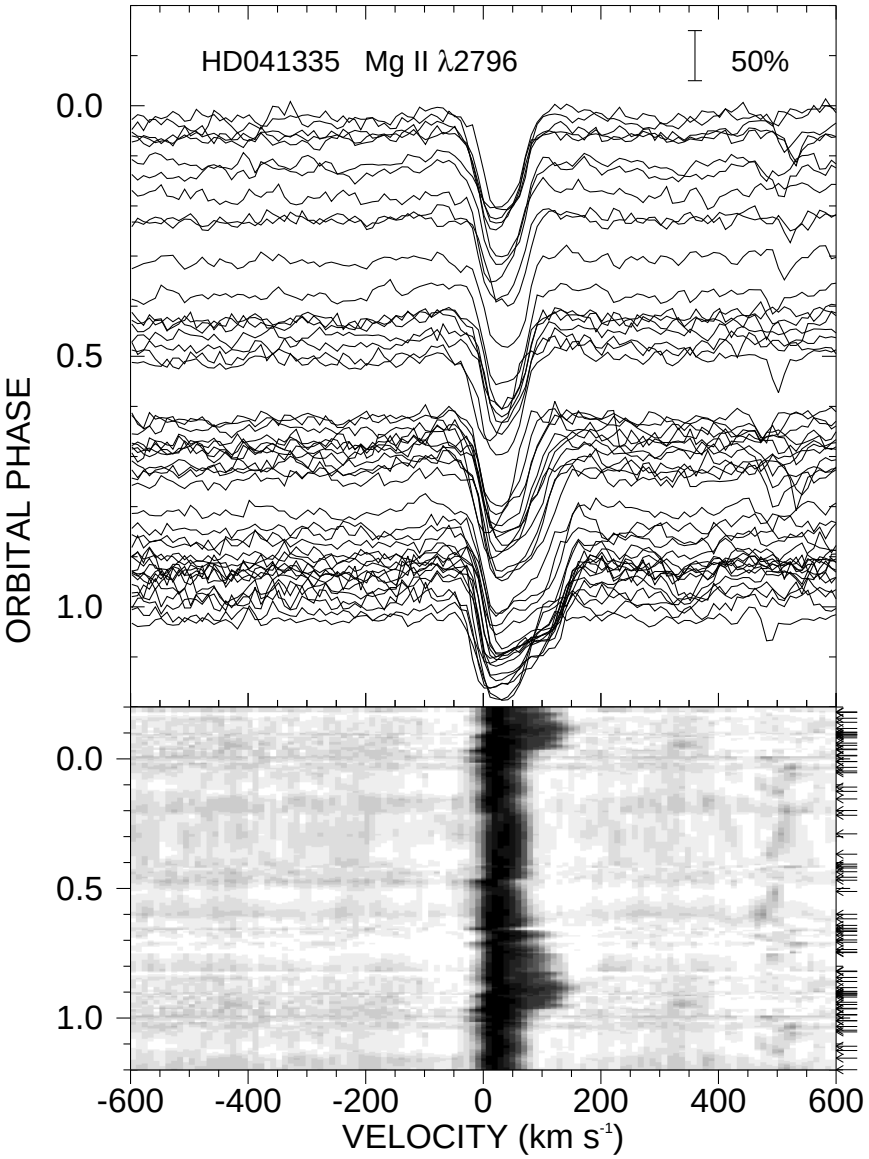

Fig. 3.17.— The top panel shows the individual spectra of Mg II λ2796.352 plotted as a function of radial velocity and orbital phase (such that the continuum is aligned with the phase of observation). The spectral flux depth relative to the continuum is indicated by the scale bar in upper right. The lower panel shows the same interpolated in orbital phase and portrayed as a gray scale image (black corresponding to deepest absorption and white to strongest continuum flux). The actual phases of observation are indicated by arrows on the right hand side.

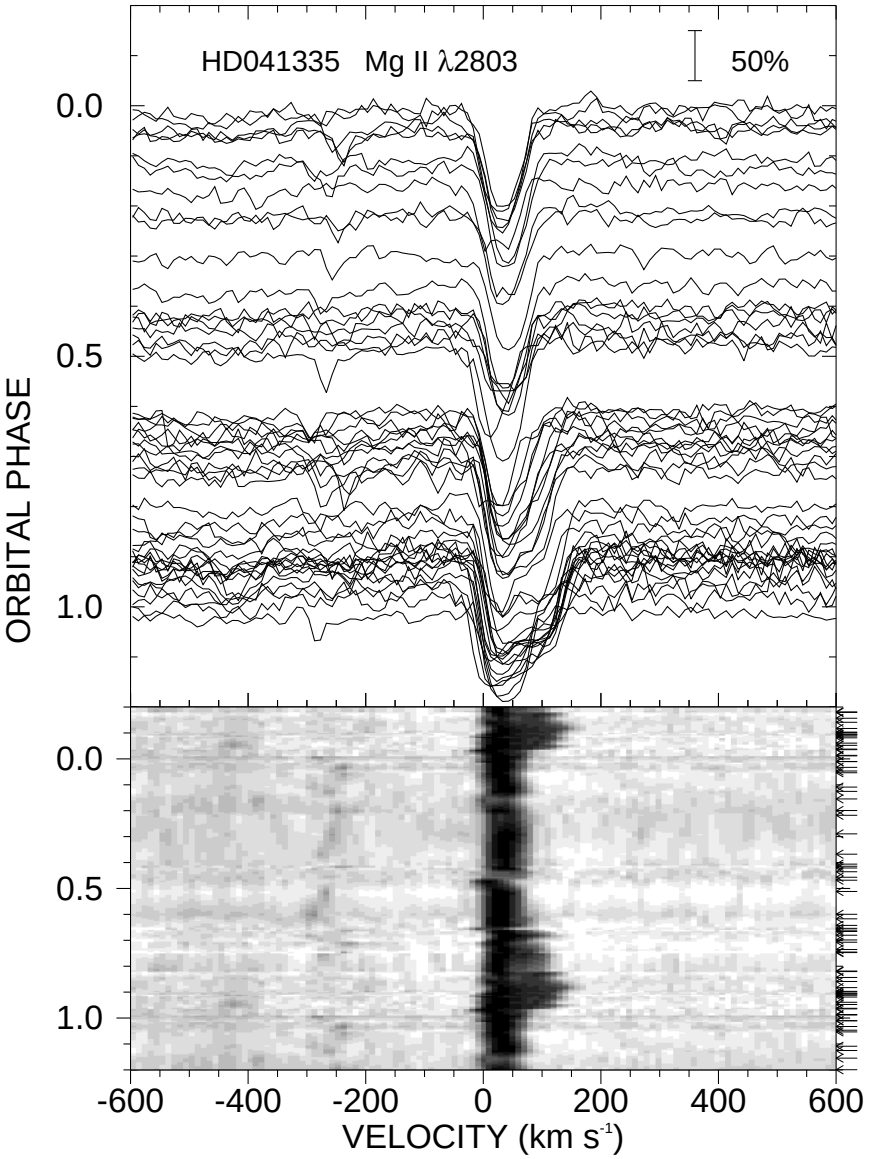

Fig. 3.18.— The top panel shows the individual spectra of Mg II λ2803.531 plotted as a function of radial velocity and orbital phase (such that the continuum is aligned with the phase of observation). The spectral flux depth relative to the continuum is indicated by the scale bar in upper right. The lower panel shows the same interpolated in orbital phase and portrayed as a gray scale image (black corresponding to deepest absorption and white to strongest continuum flux). The actual phases of observation are indicated by arrows on the right hand side.

We also observe several variations on the basic shell feature theme. Some of the weaker, lower opacity lines of low ionization species only display a limited shell feature very close to the phase of maximum absorption depth observed in Si II λ1264, $\phi = 0.95$. Examples include S II λ1250 (Fig. 3.3), Si II λ1304 (Fig. 3.7), and Si II λ1526 (Fig. 3.11). The strong resonance lines formed in the stellar wind of the Be star are Si IV λ1393 (Fig. 3.9), Si IV λ1402 (Fig. 3.10), and C IV $\lambda\lambda$1548, 1550 (Fig. 3.12). These lines have blue absorption wings that extend to -600 km s^{-1}. The cores of the wind lines also show evidence of the shell component (particularly on the less blended, positive velocity side of the line core) that is is relatively strong over the phase range $\phi = 0.6$ to 0.1. **It is striking that the shell components appear over a wide range of atomic ionization states (for example, Si II, Si III, and Si IV). This may be the result of the ionizing flux of the hot companion (Section 3) and/or shock heating related to gas flows in the vicinity of the companion (Section 5).** Finally we observe another kind of blue-shifted, shell absorption feature around the opposite conjunction at $\phi = 0.5$ that extends to $V_r = -80$ km s^{-1} in the C II $\lambda\lambda$1334, 1335 doublet (Fig. 3.8). This component was first noted by Paterson-Beeckmans (1980) who suggested that it might originate in outflow through the external Lagrangian point in the direction away from the companion. This blue-shifted shell component is also observed in the lines Al III λ1854 (Fig. 3.14), Al III λ1862 (Fig. 3.15), and Fe III λ1895 (Fig. 3.16).

Peters (1983) originally discussed the shell line appearance in the optical H Balmer lines, so for completeness, we show the orbital variations of the Hα emission line in Figure 4. This figure was constructed from the KPNO observations (Table 1) after deletion of several spectra where the emission was weaker than average. The overall appearance is similar to that reported in the past (Hanuschik et al. 1996; Pollmann 2007). The variations are less pronounced in Hα presumably because it forms over a large volume in the Be star disk, but the *primary shell phase* of increased, red-shifted absorption is clearly evident near $\phi = 0.95$. There are also hints of moving absorption sub-features that begin blue-shifted near $V_r = -100$ km s^{-1} at phases 0.0 and 0.5 that progress to line center half an orbit later. We discuss the possible origin of all these features in the next section.

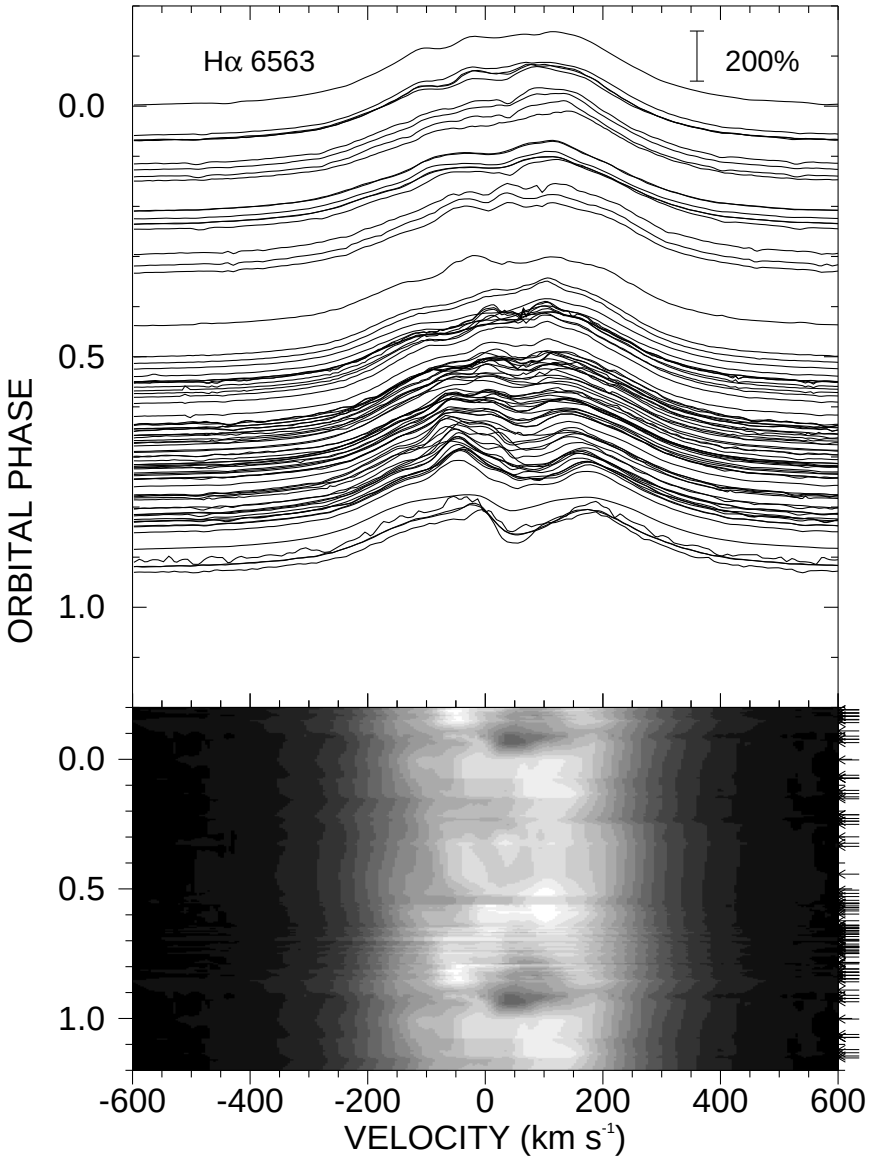

Fig. 4.— The top panel shows the individual spectra of Hα plotted as a function of radial velocity and orbital phase (such that the continuum is aligned with the phase of observation). The spectral flux depth relative to the continuum is indicated by the scale bar in upper right. The lower panel shows the same interpolated in orbital phase and portrayed as a gray scale image (black corresponding to lowest absorption and white to strongest continuum flux). The actual phases of observation are indicated by arrows on the right hand side.

5. Circumbinary Disk Model

The fact that the orbital variations of the shell lines peak in strength near the conjunction phases indicates an origin related to the presence of the companion star. Peters (1983) originally suggested that the companion was large, filling its Roche lobe, and that the primary shell phase absorption occurred in a gas stream from the companion to the Be star. However, our detection of the FUV spectrum of the companion (Section 3) shows that the companion is much smaller than its Roche lobe. Thus, here we present a different model that is based upon the idea that the companion creates a radial gap in the disk of the Be star and that the shell absorptions[6] are formed through the opacity of gas streams that are crossing the gap. We refer to this scenario as a circumbinary disk model in which the net outward motion of the disk gas extends beyond the dimensions of the binary.

The elements of the circumbinary disk model are sketched in a polar view diagram of the system in Figure 5. We set the dimensions of the binary using the projected semimajor axis $a_1 \sin i$ from Table 3, the mass ratio $q = 0.07 \pm 0.02$ from Section 3, and an orbital inclination of $i = 85°$ (high enough to permit structures close to the disk to be projected against the disk of the Be star from our line of sight). This results in a semimajor axis of $a = 0.82$ AU ($176 R_\odot$). Figure 5 shows the Be star at the origin (outlined for a radius of $5 R_\odot$) with the tiny companion at position $(x, y) = (+a, 0)$. Small arrows from each component indicate their relative orbital motion, although this is so small for the Be primary that only the arrowhead shows. The small plus sign on the axis joining the components marks the center of mass position. Tick marks appear on the periphery at intervals of $a/2$, and orientations of the view from Earth are marked by the orbital phases near the edges. The dashed line indicates the Roche lobes, and both stars are well within their respective Roche lobe boundaries.

The shaded regions indicate the Be star disk. The darkest gray portion close to the Be star illustrates the $9.5 R_\star$ boundary that we derive from the mean Hα equivalent width, $W_\lambda = -31$ Å, and the method of Grundstrom & Gies (2006). This radius represents the disk half-width at half-maximum of the intensity as seen in the plane of the sky. The disk extends beyond this radius with lower density and lower surface brightness (shown as the medium gray shaded region).

We next assume that the companion creates a gap in the disk in the same way as do planets in protoplanetary disks (Bate et al. 2003). We adopt the simplest approximation that the size of the gap is equal to the companion's Roche lobe dimensions along the axis joining

[6]In this discussion we focus on the phase-dependent variations in the shell lines. A corresponding broad underlying absorption is also observed in some lines which may be formed through another mechanism.

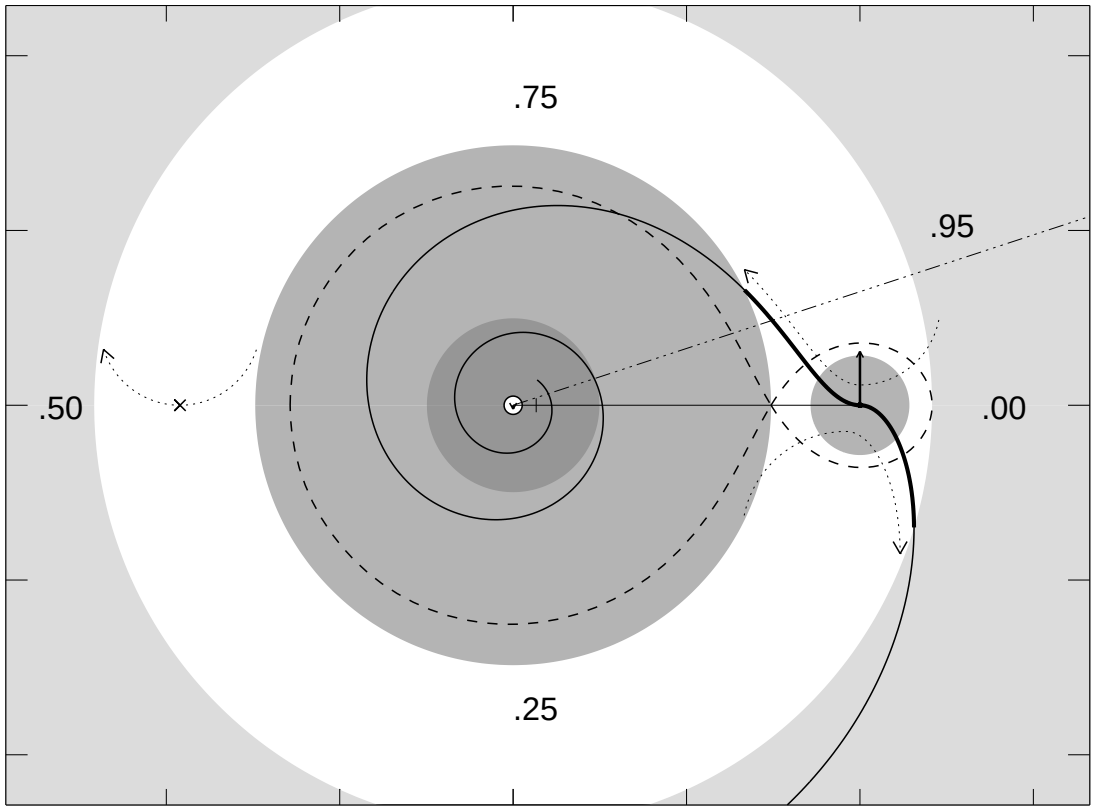

Fig. 5.— A sketch of the main components of HR 2142 as viewed from above the orbital plane. Tick marks on the axes occur at spacings of half the semimajor axis. The white circle immediately left of the center of mass (plus sign) represents the Be star, and the surrounding dark and medium gray zones represent the dense and extended regions of its circumstellar disk. The medium gray zone to the right represents the accretion disk of the hot companion, while the outer light gray region represents the circumbinary disk. The dashed line shows the Roche lobe boundaries, and we assume that the companion forms a gap in the disk that is equal in size to the long axis of the companion's Roche lobe. The spiral lines show the tidal shock location from the analytical expression from Ogilvie & Lubow (2002). Dotted lines with arrows indicate suggestive flowlines across the gap in the vicinity of the companion (right) and L3 (left, shown by a cross sign). Orbital phases for the direction of our line of sight are indicated around the periphery, and the dashed-dotted line shows the sight line to the Be star at $\phi = 0.95$ when the shell lines are strongest.

the stars. The white region in Figure 5 illustrates the gap. Beyond the gap, we imagine that the disk gas accumulates and continues again with lower density and an outwardly directed flow (shown as the light gray region at the periphery of the diagram).

Low mass companions orbiting within disks create tidal shocks in the disk gas through their gravitational perturbation of the Keplerian motion (Ogilvie & Lubow 2002; Bate et al. 2003). We calculated the position of a one-armed spiral wake using the two-dimensional approximation given by Ogilvie & Lubow (2002) (see their equations 13 and 24 for the outer and inner portions, respectively). These curves depend only on a parameter ϵ that is equal to the ratio of the gas sound speed to the circular Keplerian velocity of the companion around the primary. We assumed a sound speed of 14 km s^{-1} based upon an adopted disk gas temperature of 15 kK ($\approx 0.6 T_{\rm eff}$) and a mean molecular weight of $\mu = 0.66$. Then for a companion velocity of V(relative) $\approx$ 100 km s^{-1}, we find $\epsilon = 0.12$ (close to the $\epsilon = 0.1$ case shown in Fig. 5 of Ogilvie & Lubow 2002). The tidal wakes are shown as solid lines that cross through the position of the companion star. We extended the tidal wake curve well into the interior of the Be star disk, but we suspect that the wake density enhancement drops closer to the Be star because of gas turbulence in the disk.

The thickest portion of the wake marks those sections where we expect the density enhancements are the greatest and, hence, where the gas is located that may cause the shell line episodes. The dotted lines above and below the companion show the flow lines of gas crossing the gap due to the gravitational pull of the companion. These are parts of so-called "horseshoe orbits" that are well known in the restricted three-body problem (Dermott & Murray 1981). For example, gas at the outer edge of the gap ahead of the companion will be pulled inwards by the companion's gravity. Then by conservation of angular momentum, the azimuthal speed around the Be star increases, so the gas moves ahead of the companion and forms the wake at the inner edge of the gap. In a similar way, gas at the inner edge of the gap that is approaching the companion (below it in the diagram) will be pulled outwards toward the companion. Here conservation of angular momentum causes this gas to slow in azimuthal speed, and it falls behind the companion to strike the outer gap edge at the outer wake. Small arrows attached to each dotted line indicate the relative sense of motion in the frame of the binary.

Thus, we suspect that the main red-shifted shell feature that we see around phase $\phi = 0.95$ is due to our view of the Be star as seen through the inner tidal wake where gas is moving inward towards the Be star (and away from us). This is probably the strongest and longest duration shell phase because the gas is striking more dense gas in the inner region and over a larger wake angle relative to the Be star. Then the second blue-shifted shell phase occurs for a short time after phase 0.0 as we view the Be star flux through the

outward moving gas in the outer wake. The portions of the wake that are most important for the shell line formation are indicated with extra line thickness.

We suggest that the *primary shell phase* absorptions occur as we view the Be star through inward crossing gas that creates shocks and high density regions in the vicinity of the tidal wake spiral arm. Beginning shortly after orbital phase $\phi = 0.5$ we see the tidal wake gas projected against the Be star with a modest velocity towards the Be star (and away from us), and as the companion moves into the foreground, we observe progressively larger inflow velocities that peak near $\phi = 0.95$ (shown by the dashed-dotted line of sight in Fig. 5). This line of sight corresponds approximately to the location of the intersection of the tidal wake with the outer boundary of the inner disk. Three-dimensional simulations of gas motions in the vicinity of the tidal wake and companion by Bate et al. (2003) indicate that the inner shock region may attain a significant distance above the orbital plane that amounts to several disk scale heights. Consequently, we expect that shock structures in the disk could be seen projected against the Be star even if the orbital inclination is somewhat less than 90°.

The models by Bate et al. (2003) show that some gap crossing gas will flow into an accretion disk around the companion, and we have indicated a possible accretion disk around the companion as the medium shaded gray circle. Such an accretion disk may partially account for the apparent obscuration of the flux of the hot companion. Inward crossing gas ahead of the companion might encounter the outer regions of the accretion disk and attain a velocity comparable to the local Keplerian motion around the companion. For example, at a distance of $0.08a$ ahead of the companion, the accretion disk orbital velocity would be ≈ 100 km s^{-1} directed towards the Be star, which is comparable to the observed maximum red-shift velocity of the shell lines.

We suspect that the inner disk gas crosses the gap to the outer circumbinary disk along the axis joining the stars where the gravitational potential is most favorable. The *secondary shell phase* that occurs immediately after orbital phase $\phi = 0.0$ probably results as we view the Be star through outwardly moving (blue-shifted) dense gas at the intersection of the tidal wake and the inner boundary of the outer disk. Similarly, the short episode of blue-shifted absorption observed near phase $\phi = 0.5$ may result from gas that crosses the gap near the L3 Lagrangian point and forms a density enhancement where it strikes the outer disk. We speculate that the weak, blue-shifted and migrating sub-features in Hα that begin at each conjunction originate in tidal wakes in the outer circumbinary disk.

Our schematic model in Figure 5 must be only an approximation of the actual disk structure, and fortunately there are a number of numerical simulations by Okazaki et al. (2002) and Panoglou et al. (2016) that use three-dimensional,

smoothed particle hydrodynamical codes to model the disks of Be stars in binary systems. These show that the presence of the companion creates a disk truncation radius that is somewhat smaller than the Roche radius of the Be star R_L, i.e., between $0.7R_L$ for truncation at the 4:1 period resonance ratio (Okazaki et al. 2002) and $0.8R_L$ for truncation at the 3:1 period resonance ratio (Panoglou et al. 2016) depending on the disk viscosity. Consequently, the inner gap boundary plotted in Figure 5 may be somewhat large. The inner tidal wake shown in Figure 5 is also found in the circular orbit simulations of Panoglou et al. (2016) (described there as a spiral arm), and the geometry of wake in the simulations (for a ratio of sound speed to companion orbital velocity of $\epsilon = 0.08$) agrees well with the analytical formula (compare Fig. 4 of Panoglou et al. 2016 with Fig. 5 of Ogilvie & Lubow 2002). However, the numerical models do not show evidence of an outer disk, i.e., instead of a gap there is simply one truncation of the Be star disk. This is partially due to the nature of the simulations that are focused on the inner structure of the disk and not on the gas flows in the vicinity of the secondary (where the timescales are too short for efficient numerical resolution). Nevertheless, we anticipate that future simulations will document the outward leakage of disk gas, which carries away the angular momentum shed by the Be star, in such a way that gas is preferentially lost along the axis joining the stars into a circumbinary disk (for example, as is predicted in Roche lobe overflow systems; Nazarenko & Glazunova 2006).

6. Conclusions

Our investigation of the UV and optical spectrum of HR 2142 has led to a new understanding of the nature of this binary system and its circumbinary disk. We used the revised spectroscopic orbit of the Be star to establish the orbital geometry and to predict the radial velocity of the faint companion at the times of observation. These predicted Doppler shifts were applied to cross-correlation functions of the far-UV spectra of HR 2142 with a model spectrum for a hot companion, and the shift-and-added CCFs reveal a faint peak caused by the spectral features of the companion. The companion is a hot and small subdwarf, the stripped down remains of the originally more massive star in this system that transferred both mass and angular momentum to the Be star. Our current results lead to mass estimates of $9M_\odot$ and $0.7M_\odot$ for the Be star and hot companion, respectively. Future observations of the orbital motion of the distant tertiary companion of HR 2142 (ESA 1997; Horch et al. 2002; Oudmaijer & Parr 2010) will help establish the total system mass.

HR 2142 is now the fourth Be+sdO system where UV spectroscopy has led to the detection of the spectral contribution of the hot companion (Gies et al. 1998; Peters et al. 2008, 2013). The hot subdwarf is small, $R_2/R_\odot > 0.13$, and it has a relatively low luminosity, $\log L/L_\odot > 1.7$. In fact, the companion may have a mass and radius typical of a white dwarf (Provencal et al. 1998), although it is much hotter than most. Binary evolutionary models may help determine if the hot companion of HR 2142 is still in a core He burning stage or some more advanced stage (A. Schootemeijer et al., in preparation).

We have documented the orbital variations of the shell line absorptions in the UV spectrum and Hα, and we suggest that these are formed mainly in dense gas regions where a tidal wake caused by the companion intersects with boundaries of a gap in the disk of the Be star. Shocks are formed in these regions as gas crossing the gap strikes the dense gas of the disk, and the resulting shock heating helps to explain the presence of the shell components in high ionization species like Si IV and C IV. It may be possible in the future to detect the gap in the disk and the tidal wake regions through high angular resolution observations with optical long baseline interferometry. **Furthermore, the heated tidal wake regions may be responsible for the emission line formation in the vicinity of the companion that is observed in some Be+sdO binaries (in addition to direct heating by the flux of the companion; Hummel & Štefl 2001). The He I λ6678 emission line shows evidence of localized heating in the cases of ϕ Per (Štefl et al. 2000), FY CMa (Peters et al. 2008), and 59 Cyg (Peters et al. 2013), so we might expect similar emission variations in the spectrum of HR 2142. There is some evidence of a variable emission component that fills in the wide absorption profile of He I λ6678 in our spectra, but it is much weaker than observed in the other Be+sdO systems, perhaps due to the lower luminosity of the subdwarf.**

It was the remarkable orbital variations in the shell line spectrum that first drew our attention to HR 2142 (Peters 1971, 1972). If the circumbinary disk model of gap crossing gas is applicable to other Be+sdO binaries, then we might naively expect that they should also display such shell line variations in their spectra. However, to our knowledge the appearance of shell lines near Be star superior conjunction has only been reported for the sudden appearance of Fe IV lines in the FUV spectrum of ϕ Per (Gies et al. 1998). We speculate that tidal wakes may occur in other Be binaries, but that they only present observable shell lines if (1) the Be star's disk is particularly massive and has substantial density out to the vicinity of the companion, (2) the orbital inclination is close to $i = 90°$ so that the disk perturbations caused by the tidal wakes reach to a vertical displacement that occults our line of sight to the Be star, and (3) the companion is not so massive that it creates a gap that is too wide to facilitate gas

migration across the gap. HR 2142 may represent a fortuitous conjunction in which all three conditions appear to be met. The example of HR 2142 illustrates the importance of binary Be stars as laboratories for investigations of disk dynamical processes.

Some of the data presented in this paper were obtained from the Mikulski Archive for Space Telescopes (MAST). STScI is operated by the Association of Universities for Research in Astronomy, Inc., under NASA contract NAS5-26555. Support for MAST for non-HST data is provided by the NASA Office of Space Science via grant NNX09AF08G and by other grants and contracts. This work has made use of the BeSS database, operated at LESIA, Observatoire de Meudon, France: http://basebe.obspm.fr. Our work was supported in part by NASA grant NNX10AD60G (GJP) and by the National Science Foundation under grant AST-1411654 (DRG). Institutional support has been provided from the GSU College of Arts and Sciences, the Research Program Enhancement fund of the Board of Regents of the University System of Georgia (administered through the GSU Office of the Vice President for Research and Economic Development), and by the USC Women in Science and Engineering (WiSE) program (GJP).

Facilities: IUE, KPNO:CFT

REFERENCES

Bate, M. R., Lubow, S. H., Ogilvie, G. I., & Miller, K. A. 2003, MNRAS, 341, 213

Campbell, W. W. 1895, ApJ, 2, 177

de Mink, S. E., Sana, H., Langer, N., Izzard, R. G., & Schneider, F. R. N. 2014, ApJ, 782, 7

Dermott, S. F., & Murray, C. D. 1981, Icarus, 48, 1

Duchêne, G., & Kraus, A. 2013, ARA&A, 51, 269

ESA, ed. 1997, ESA Special Publication, Vol. 1200, The HIPPARCOS and TYCHO catalogues. Astrometric and photometric star catalogues derived from the ESA HIPPARCOS Space Astrometry Mission

Frémat, Y., Zorec, J., Hubert, A.-M., & Floquet, M. 2005, A&A, 440, 305

Gies, D. R., Bagnuolo, Jr., W. G., Ferrara, E. C., et al. 1998, ApJ, 493, 440

Grundstrom, E. D., & Gies, D. R. 2006, ApJ, 651, L53

Hanuschik, R. W., Hummel, W., Sutorius, E., Dietle, O., & Thimm, G. 1996, A&AS, 116, 309

Horch, E. P., Robinson, S. E., Meyer, R. D., et al. 2002, AJ, 123, 3442

Hummel, W., & Štefl, S. 2001, A&A, 368, 471

Koubský, P., Kotková, L., Votruba, V., Šlechta, M., & Dvořáková, Š. 2012, A&A, 545, A121

Koubský, P., Kotková, L., Kraus, M., et al. 2014, A&A, 567, A57

Lanz, T., & Hubeny, I. 2003, ApJS, 146, 417

Morbey, C. L., & Brosterhus, E. B. 1974, PASP, 86, 455

Morton, D. C., York, D. G., & Jenkins, E. B. 1988, ApJS, 68, 449

Mourard, D., Monnier, J. D., Meilland, A., et al. 2015, A&A, 577, A51

Nazarenko, V. V., & Glazunova, L. V. 2006, Astronomy Reports, 50, 369

Neiner, C., de Batz, B., Cochard, F., et al. 2011, AJ, 142, 149

Ogilvie, G. I., & Lubow, S. H. 2002, MNRAS, 330, 950

Okazaki, A. T., Bate, M. R., Ogilvie, G. I., & Pringle, J. E. 2002, MNRAS, 337, 967

Oudmaijer, R. D., & Parr, A. M. 2010, MNRAS, 405, 2439

Panoglou, D., Carciofi, A. C., Vieira, R. G., et al. 2016, ArXiv e-prints

Paterson-Beeckmans, F. 1980, in ESA Special Publication, Vol. 157, 2nd European IUE Conference, ed. B. Battrick & J. Mort, 51–54

Peters, G. J. 1971, ApJ, 163, L107

—. 1972, PASP, 84, 334

—. 1983, PASP, 95, 311

—. 2001, Publications of the Astronomical Institute of the Czechoslovak Academy of Sciences, 89, 30

Peters, G. J., & Gies, D. R. 2002, in Astronomical Society of the Pacific Conference Series, Vol. 279, Exotic Stars as Challenges to Evolution, ed. C. A. Tout & W. van Hamme, 149

Peters, G. J., Gies, D. R., Grundstrom, E. D., & McSwain, M. V. 2008, ApJ, 686, 1280

Peters, G. J., Gies, D. R., Wang, L., & Grundstrom, E. D. 2015, in IAU Symposium, Vol. 307, IAU Symposium, ed. G. Meynet, C. Georgy, J. Groh, & P. Stee, 131–132

Peters, G. J., Pewett, T. D., Gies, D. R., Touhami, Y. N., & Grundstrom, E. D. 2013, ApJ, 765, 2

Poeckert, R. 1981, PASP, 93, 297

Pollmann, E. 2007, Information Bulletin on Variable Stars, 5778, 1

Pols, O. R., Cote, J., Waters, L. B. F. M., & Heise, J. 1991, A&A, 241, 419

Provencal, J. L., Shipman, H. L., Høg, E., & Thejll, P. 1998, ApJ, 494, 759

Reig, P. 2011, Ap&SS, 332, 1

Rivinius, T., Carciofi, A. C., & Martayan, C. 2013, A&A Rev., 21, 69

Shafter, A. W., Szkody, P., & Thorstensen, J. R. 1986, ApJ, 308, 765

Shao, Y., & Li, X.-D. 2014, ApJ, 796, 37

Thaller, M. L., Bagnuolo, Jr., W. G., Gies, D. R., & Penny, L. R. 1995, ApJ, 448, 878

Štefl, S., Hummel, W., & Rivinius, T. 2000, A&A, 358, 208

Waters, L. B. F. M., Cote, J., & Pols, O. R. 1991, A&A, 250, 437

Wellstein, S., Langer, N., & Braun, H. 2001, A&A, 369, 939

This preprint was prepared with the AAS LaTeX macros v5.2.